

Large-eddy simulation of bubble plume in stratified crossflow

Shuolin Xiao, Chen Peng, and Di Yang ^{*}*Department of Mechanical Engineering, University of Houston, Houston, Texas 77204, USA*

(Received 8 March 2020; accepted 7 April 2021; published 29 April 2021)

Characteristics and material transport of a bubble-driven plume in stably stratified water with uniform crossflow are studied using an Eulerian-Eulerian large-eddy simulation model. Four laboratory-scale plume conditions with different bubble rise velocities ($w_r = 3, 6, 12,$ and 20 cm/s) are considered, and their characteristics under three weak crossflow conditions ($U_c = 0.5, 1,$ and 2 cm/s) are studied. The interaction between the rising bubbles and the stratified water generates a double-plume structure, consisting of a rising plume of bubble/water mixture and a falling plume of dense water peeled from the rising plume due to the stratification effect. The presence of crossflow forces the rising plume to incline and causes the falling plume to form on the downstream side (with respect to the crossflow direction) of the rising plume, resulting in reduced contact area between the two plumes. Consequently, the turbulent mixing of the vertical momentum between the rising and falling plumes is reduced, causing the magnitude of the vertical velocity in both plumes to increase when the crossflow velocity is increased. The material transport from the plume to the horizontal intrusion layer (traced using dye) also exhibits strong dependence on the crossflow velocity. Faster crossflow results in narrower lateral extension and wider vertical extension of the intrusion layer due to the interaction between the peeling process and the crossflow. For cases with the two smaller w_r (3 and 6 cm/s), the plume can form a distinct peeling event that dominates the material transport process. As a result, the mean intrusion layer height h_t shows only small variation for these two plume conditions when U_c is increased. In contrast, the plumes with $w_r = 12$ and 20 cm/s exhibit noticeable decrease of h_t (9% and 24%, respectively) when U_c is increased from 0.5 to 2 cm/s. Statistical analysis of the streamwise dye flux shows that the decrease of h_t with increased U_c for the cases with $w_r = 12$ and 20 cm/s is mainly due to the crossflow-enhanced mean flux of dye from the rising plume at the low elevation.

DOI: [10.1103/PhysRevFluids.6.044613](https://doi.org/10.1103/PhysRevFluids.6.044613)

I. INTRODUCTION

When bubbles are released into the water, they drive the surrounding water to rise together as a multiphase plume. Underwater release of multiphase bubble/water mixed plume can occur naturally (e.g., natural petroleum seeps from seafloor [1,2]), artificially (e.g., reservoir destratification and aeration systems [3–6]), or accidentally (e.g., subsea wellhead blowout accidents [7,8]). The dynamics of the bubble-driven plume near the source of the subsea release is strongly affected by the bubble-induced buoyancy effect and the stable water stratification [4,9,10]. During the plume rising process, ambient water gets entrained into the plume by the turbulent eddies at the edge of the plume and lifted to higher elevations. In a stably stratified water environment (i.e., the water density decreases gradually towards higher elevation), the net buoyancy of the plume decreases with height due to the increasing density difference between the lifted water within the plume and ambient water

^{*}diyang@uh.edu

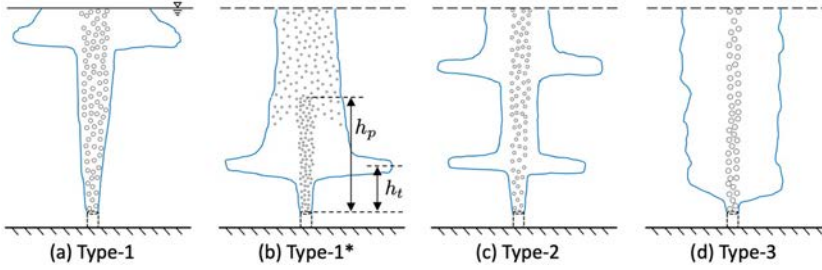


FIG. 1. Schematics of plume structure types in stratified water without crossflow based on the plume classification defined by Asaeda and Imberger [4] and Socolofsky *et al.* [12].

around the plume. The reduced buoyancy eventually results in the peeling of the entrained water at a height of maximum rise (named the peel height, h_p), and a falling plume is formed outside the rising inner plume [4,9,10]. The peeled water falls as a downward plume to a neutral buoyancy level (named the trap height, h_t), and then disperses horizontally to form an intrusion layer [4,11].

Asaeda and Imberger [4] performed water tank experiments of bubble-driven plumes in stratified water without crossflow and classified the plume structures into three types. In this classification, the Type 1 plume has a large gas flow rate and weak stratification, allowing the plume to reach the water surface directly without forming the peeling event [Fig. 1(a)]; the Type 2 plume has moderate gas flow rate and water stratification, resulting in distinct peeling events to form stable intrusion layers [Fig. 1(c)]; the Type 3 plume has low gas flow rate and strong stratification, resulting in irregular peeling process and unstable intrusion [Fig. 1(d)].

By performing a large set of laboratory experiments, Socolofsky *et al.* [12] and Socolofsky and Adams [9,11] further extended and generalized the plume classification of Asaeda and Imberger [4]. They found that the plume structure can be classified based on a key dimensionless parameter, the dimensionless bubble rise velocity, defined as [9,11,12]

$$W_N = w_r / (B_0 N)^{1/4}, \quad (1)$$

where w_r is the bubble rise velocity, B_0 is the kinematic buoyancy flux induced by the bubble source, and N is the buoyancy frequency of the stratified water. For fixed B_0 and N , the value of W_N increases when w_r increases, which can be realized by increasing the size of the released bubbles. Socolofsky and Adams [9,11] conducted their experiments with sufficient water depth so that the Type 1 plume [Fig. 1(a)] did not occur. Instead, they observed a new Type 1* plume when $W_N < 1.5$ [9], which usually occurs when the plume is driven by small bubbles that have small rise velocity relative to the surrounding water. As illustrated in Fig. 1(b), the small bubbles accumulate above the source to form a strong buoyancy flux and drive the plume to rise. When the plume reaches the peeling region, the lateral flow motions associated with the peeling process widen the bubble plume diameter and reduce the bubble mass concentration. Above the peel height, although the small bubbles can continue to drive the plume, the reduced bubble mass concentration results in a weakened buoyancy that is insufficient to form distinct intrusion above the first peel height. As the dimensionless rise velocity further increases to $1.5 < W_N < 2.4$ [9], the plume falls into the Type 2 category [Fig. 1(c)]. The major difference between the Type 2 and Type 1* plumes is that the bubbles in the Type 2 plume have sufficient buoyancy and rise velocity to resist the lateral diffusion at the peel height and maintain the bubble concentration beyond the first peel height, which allows the formation of successive intrusion layers if the water depth is sufficient [Fig. 1(c)]. As W_N further increase to $W_N > 2.4$ (usually for plume with large bubbles), the plume becomes the Type 3 with irregular peeling and unsteady intrusion [9]. This plume classification based on W_N [9,11,12] has been successfully applied to classify the plume structures in several recent studies (see, e.g., Refs. [10,13–16]).

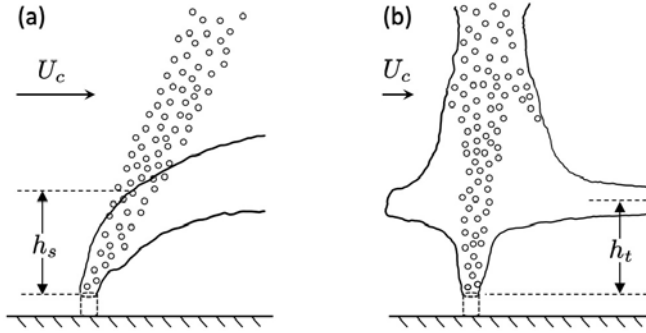


FIG. 2. Schematics of plume structures in stratified water with (a) strong and (b) weak crossflows. U_c denotes the crossflow velocity, h_s denotes the height where the bubble and water plumes separate [19], and h_t denotes the trap height of the detrained water [11,19].

In an open water environment, crossflow often occurs and can further complicate the dynamics of the bubble-driven multiphase plume (see, e.g., Refs. [8,10,17,18]). As shown in Fig. 2(a), a strong crossflow can tilt the bubble plume and entrained water stream in the multiphase plume at different angles away from the vertical direction due to their different vertical velocities, causing them to quickly separate at a critical height h_s above the plume source [19]. As illustrated in Fig. 2(a), this separation height h_s is defined as the height where the upper bound of the water stream separates from the centerline of the bubble plume [10,19]. After the separation from the bubble plume, the further transport of the water stream may be tracked and modeled relatively easily without the influence of the bubble buoyancy [18]. If the crossflow is relatively weak [Fig. 2(b)], the bubbles and the entrained water flow in the plume cannot be separated directly by the crossflow before the multiphase plume reaches the peel height [19], resulting in inclined rising/falling double-plume structure with increased complexity in the plume dynamics due to the crossflow. Socolofsky and Adams [19] performed a series of experiments to study bubble-driven plumes in both unstratified and stratified crossflows. They observed the plume structures from the side using the laser-induced fluorescence method. It should be noted that most of their reported experiments were for plumes in unstratified crossflow, and only four exploratory cases (no crossflow as well as weak, moderate, and strong crossflows) with water stratification were included to illustrate the complex plume dynamics in stratified crossflow. Although these limited number of experiments provided valuable insights about the macroscopic plume structures in stratified crossflow, they did not provide the three-dimensional characteristics of the plumes or the quantitative information of the velocity and dye concentration fields. To date, there is a lack of systematic investigation on the characteristics of buoyant plumes in stratified crossflows (see the recent review by Boufadel *et al.* [20]), and the detailed plume dynamics and material transport under the combined influence of stratification and crossflow are still not well understood.

In recent years, large-eddy simulation (LES) has become a valuable numerical tool for modeling the detailed turbulent flow physics in buoyant plumes (see, e.g., Refs. [21–28]). LES captures the unsteady turbulent plume dynamics over a range of spatial and temporal scales down to the computational grid scale, and models the unresolved small-scale effects using the subgrid-scale (SGS) models [29]. Among different strategies for modeling the multiphase bubble-driven plumes, the Eulerian-Eulerian approach [30,31] has been widely adopted due to its relatively low computational cost [20,32]. In the Eulerian-Eulerian approach, the water in and around the plume is treated as a continuous phase and its turbulent flow motions are modeled in LES by solving the filtered Navier-Stokes equations; the bubble field is treated as a dispersed particle phase and described using an Eulerian concentration function, and its evolution is modeled by solving a filtered advection-diffusion equation. The Eulerian-Eulerian LES approach has been successfully applied in

several recent studies to model the buoyant multiphase plumes in stratified water environment (see, e.g., Refs. [14,15,24,25,28,33,34]).

In this study, the dynamics of bubble-driven plume in stably stratified water with crossflow is modeled using the Eulerian-Eulerian LES bubble plume model developed in Yang *et al.* [14]. The simulations focus on conditions with relatively weak crossflow, aiming at capturing the rich dynamics of the plume when it is affected by both the stratification and the crossflow. Three different crossflow velocities are considered: $U_c = 0.5, 1, \text{ and } 2 \text{ cm/s}$. For each crossflow velocity, four plume conditions with different bubble rise velocities are considered, $w_r = 3, 6, 12, \text{ and } 20 \text{ cm/s}$, for which the corresponding dimensionless rise velocity based on Eq. (1) are $W_N = 0.53, 1.06, 2.12, \text{ and } 3.53$, respectively. As discussed in detail in Sec. III, these simulation cases are set up such that the weak crossflow does not force the bubbles and the entrained water stream to separate too early, allowing the bubble/water mixed plume to have sufficient interaction with the stratified water to reach the peel height and form the falling plume [Fig. 2(b)]. Moreover, a reference case without crossflow is also simulated for $w_r = 6 \text{ cm/s}$ for comparison purpose. Based on the LES results, both the instantaneous and time-averaged plume structures from the various simulation cases are compared to elucidate the effects of crossflow on the plume characteristics. The interactions of the bubble-driven plume with water stratification and crossflow also strongly affect how materials carried by the plume are dispersed into the surrounding water. To track the material transport process, a dye tracer is released into the plume and its transport is simulated in the LES by solving the filtered advection-diffusion equation for the dye concentration. The statistics of the dye fluxes due to both the mean flow and turbulence are quantified, and the results for different simulation cases are compared in this paper. By performing these systematic simulations and data analysis, this study aims at characterizing the combined effects of stable stratification and weak crossflow on the plume structure and the material transport under various bubble and crossflow conditions.

The remainder of this paper is organized as follows. The LES model is described in detail in Sec. II. The configurations of the simulation cases are discussed in Sec. III. The simulations and statistical analysis results are reported in Sec. IV. Finally, conclusions are given in Sec. V.

II. LARGE-EDDY SIMULATION MODEL DESCRIPTION

The present LES model uses the Cartesian coordinate system defined as $\mathbf{x} = (x, y, z)$, where x , y , and z are the streamwise, spanwise, and vertical coordinates, respectively. The corresponding velocity vector is denoted as $\mathbf{u} = (u, v, w)$. In the LES model, the bubble phase is assumed to have low void fraction and carry negligible momentum compared with the water phase [14,25,26]. The water flow in and around the plume is modeled as a continuous phase carrier flow, which is governed by the filtered Navier-Stokes equations [14,34,35],

$$\nabla \cdot \tilde{\mathbf{u}} = 0, \quad (2)$$

$$\frac{\partial \tilde{\mathbf{u}}}{\partial t} + \tilde{\mathbf{u}} \cdot \nabla \tilde{\mathbf{u}} = -\frac{1}{\rho_0} \nabla \tilde{P} - \nabla \cdot \boldsymbol{\tau}^d + \left(1 - \frac{\tilde{\rho}}{\rho_0}\right) g \mathbf{e}_z + \left(1 - \frac{\rho_b}{\rho_0}\right) \frac{\tilde{C}_b}{\rho_b} g \mathbf{e}_z. \quad (3)$$

Here, the tilde denotes the variable resolved by the LES computational grid; ρ_0 is the reference water density; $\tilde{\rho}$ is the resolved local water density; ρ_b is the density of air in the bubbles; g is the gravitational acceleration; \mathbf{e}_z is the unit vector in the vertical direction; \tilde{C}_b is the resolved mass concentration of air bubbles; $\boldsymbol{\tau}^d = \boldsymbol{\tau} - [\text{tr}(\boldsymbol{\tau})/3]\mathbf{I}$ is the deviatoric part of the subgrid-scale stress tensor $\boldsymbol{\tau} = \tilde{\mathbf{u}}\tilde{\mathbf{u}} - \tilde{\mathbf{u}}\tilde{\mathbf{u}}$, where $\text{tr}(\boldsymbol{\tau})$ is the trace of $\boldsymbol{\tau}$ and \mathbf{I} is the identity tensor; and $\tilde{P} = \tilde{p} + \rho_0[\text{tr}(\boldsymbol{\tau})/3 + (\tilde{\mathbf{u}} \cdot \tilde{\mathbf{u}})/2 - gz]$ is the modified pressure, where \tilde{p} is the resolved water pressure. The last two terms in Eq. (3) are the buoyancy forces due to water stratification and bubble concentration, respectively, which are modeled based on the Boussinesq approximation [14,15,25,28,33,34,36–38]. More details on the derivation of Eq. (3) are given in Appendix A.

Following previous LES studies (see, e.g., Refs. [14,28,33,36–38]), the water density stratification is modeled by simulating a temperature field θ governed by a filtered convection-diffusion

equation

$$\frac{\partial \tilde{\theta}}{\partial t} + \nabla \cdot (\tilde{\mathbf{u}}\tilde{\theta}) = -\nabla \cdot \boldsymbol{\pi}_\theta, \quad (4)$$

and the density field $\tilde{\rho}$ is assumed to vary linearly with $\tilde{\theta}$ as

$$\tilde{\rho} = \rho_0[1 - \alpha_t(\tilde{\theta} - \theta_0)], \quad (5)$$

where $\boldsymbol{\pi}_\theta = \tilde{\mathbf{u}}\tilde{\theta} - \tilde{\mathbf{u}}\tilde{\theta}$ is the SGS thermal flux, α_t is the thermal expansion coefficient, and θ_0 is the reference temperature corresponding to the reference water density ρ_0 .

In the present LES model, the bubbles are modeled as a dispersed phase transported by the carrier flow, with their instantaneous local concentration being described by a continuous Eulerian concentration function $C_b(\mathbf{x}, t)$. The evolution of the concentration field is simulated by solving a filtered transport equation,

$$\frac{\partial \tilde{C}_b}{\partial t} + \nabla \cdot (\tilde{\mathbf{v}}_b \tilde{C}_b) = -\nabla \cdot \boldsymbol{\pi}_b + q_b, \quad (6)$$

where $\tilde{\mathbf{v}}_b$ is the Lagrangian transport velocity of bubbles, $\boldsymbol{\pi}_b = \tilde{\mathbf{u}}\tilde{C}_b - \tilde{\mathbf{u}}\tilde{C}_b$ is the SGS flux of bubble mass concentration, and q_b is a volumetric source term representing the release of the air bubbles from a localized source (being zero outside the source region). The bubble transport velocity $\tilde{\mathbf{v}}_b$ is modeled as [14,28,39]

$$\tilde{\mathbf{v}}_b = \tilde{\mathbf{u}} + w_r \mathbf{e}_z + \frac{w_r}{g} \frac{D\tilde{\mathbf{u}}}{Dt}, \quad (7)$$

where w_r is the rise velocity of bubbles relative to the surrounding carrier flow caused by the bubble buoyancy, and $D\tilde{\mathbf{u}}/Dt = \partial\tilde{\mathbf{u}}/\partial t + \tilde{\mathbf{u}} \cdot \nabla\tilde{\mathbf{u}}$ is the material derivative (or Lagrangian acceleration) of the carrier flow velocity. Following Zheng and Yapa [40], the bubble rise velocity is parametrized based on

$$w_r = \frac{\text{Re}_b \mu}{\rho_0 d}, \quad (8)$$

where μ is the water viscosity and d is the equivalent spherical diameter of the bubble. The particle Reynolds number Re_b can be parametrized in explicit function form as [41]

$$\begin{aligned} \text{Re}_b &= N_D/24 - 1.7569 \times 10^{-4} N_D^2 \\ &\quad + 6.9252 \times 10^{-7} N_D^3 \\ &\quad - 2.3027 \times 10^{-10} N_D^4, & \text{if } N_D \leq 73, \\ \log_{10} \text{Re}_b &= -1.7095 + 1.33438W - 0.11591W^2, & \text{if } 73 < N_D \leq 580, \\ \log_{10} \text{Re}_b &= -1.81391 + 1.34671W - 0.12427W^2 \\ &\quad + 0.006344W^3, & \text{if } 580 < N_D \leq 1.55 \times 10^7, \end{aligned} \quad (9)$$

where $N_D = 4\rho_0(\rho_0 - \rho_b)gd^3/3\mu^2$ and $W = \log_{10} N_D$.

In addition, the transport of dye tracers is also simulated in the LES model to capture the effects of the plume dynamics and crossflow on transporting materials. The evolution of the dye mass concentration field \tilde{C}_{dye} is governed by the filtered transport equation

$$\frac{\partial \tilde{C}_{\text{dye}}}{\partial t} + \nabla \cdot (\tilde{\mathbf{u}}\tilde{C}_{\text{dye}}) = -\nabla \cdot \boldsymbol{\pi}_{\text{dye}} + q_{\text{dye}}, \quad (10)$$

where q_{dye} is a source term for the dye release and $\boldsymbol{\pi}_{\text{dye}} = \tilde{\mathbf{u}}\tilde{C}_{\text{dye}} - \tilde{\mathbf{u}}\tilde{C}_{\text{dye}}$ is the SGS dye concentration flux. Unlike the bubbles, the concentration function of the dye tracers is transported by the carrier flow as a passive scalar, thus the resolved carrier flow velocity $\tilde{\mathbf{u}}$ is used in the convective term in Eq. (10).

Similar to prior LES studies of turbulent plumes and jets (see, e.g., Refs. [14,15,24,25,28,33–35]), the molecular viscosity and molecular diffusivity terms are omitted in the filtered LES governing equations (3), (4), (6), and (10) due to their negligible effects compared with the corresponding SGS flux terms. The LES governing equations are closed by parametrizing the SGS terms with proper turbulence closures. In particular, the SGS stress tensor τ^d is parametrized using the Lilly-Smagorinsky eddy-viscosity type model [42,43], $\tau^d = -2\nu_{sgs}\tilde{\mathbf{S}}$, where $\tilde{\mathbf{S}} = [\nabla\tilde{\mathbf{u}} + (\nabla\tilde{\mathbf{u}})^T]/2$ is the resolved strain rate tensor, $\nu_{sgs} = (c_s\Delta)^2|\tilde{\mathbf{S}}|$ is the modeled SGS eddy viscosity, c_s is the Smagorinsky model coefficient, and Δ is the LES grid (filter) scale. The value of c_s is determined dynamically during the simulation using the Lagrangian-averaged scale-dependent dynamic (LASD) SGS model [44]. The SGS fluxes of the scalar quantities are then parametrized as $\pi_\theta = -(\nu_{sgs}/Pr_{sgs})\nabla\tilde{\theta}$, $\pi_b = -(\nu_{sgs}/Sc_{sgs})\nabla\tilde{C}_b$, and $\pi_{dye} = -(\nu_{sgs}/Sc_{sgs})\nabla\tilde{C}_{dye}$, with the constant SGS Prandtl number $Pr_{sgs} = 0.4$ and SGS Schmidt number $Sc_{sgs} = 0.4$ [14,34,35,45–50].

The present LES model uses a hybrid numerical scheme for solving the governing equations for the flow and scalar field evolutions. For the flow field, Eqs. (2) and (3) are discretized by the pseudospectral method in the horizontal directions on collocated grids and the second-order central finite difference method in the vertical direction on staggered grids [51]. The velocity field is advanced in time by the second-order Adams-Bashforth scheme. The divergence-free constraint of the velocity field is ensured by solving the pressure field from a Poisson equation constructed based on Eq. (2). The pressure is then used to project the predicted velocity field onto the divergence-free space. Equation (4) is also discretized by the hybrid pseudospectral and finite difference method and integrated in time by the second-order Adams-Bashforth scheme.

Unlike the flow equations, Eqs. (6) and (10) are for the spatially nonhomogeneous bubble and dye concentration fields and are not discretized by the pseudospectral method. Instead, they are discretized by a finite-volume method developed by Chamecki *et al.* [52], which uses the carrier flow velocity field interpolated from the pseudospectral/finite-difference flow solver's computational grids to the finite-volume grids of the scalar field solver based on a constrained interpolation scheme that conserves the velocity divergence-free condition. The LES solver for Eqs. (6) and (10) uses a bounded third-order upwind scheme for the advection term [53] and advances in time using the second-order Adams-Bashforth scheme [52]. Although the bounded finite-volume method induces additional numerical dissipation to the LES scalar solver, it provides the necessary boundedness to the simulated particle concentration field to suppress the occurrence of numerical oscillation that may result in unphysical negative concentration [52]. The present hybrid LES model uses the dissipative finite-volume method only for the particle concentration field, while uses the pseudospectral method combined with the advanced LASD SGS model to reserve the high-order accuracy of the simulated turbulent flow velocity and temperature fields. A similar hybrid LES modeling approach has been successfully applied in several prior studies of particle transport in turbulent flows and showed good agreements with experimental data and theoretical predictions (see, e.g., Refs. [35,50,54–56]).

The pseudospectral method used in the present LES is based on the Fourier series transformation, which typically requires periodic boundary conditions in the horizontal directions. In order to enable the application of inflow/outflow conditions in the streamwise direction for modeling the plume interacting with a crossflow, in this study the fringe zone method [57–59] is adopted. As illustrated in Fig. 3, a fringe zone of finite streamwise thickness adjacent to the outflow boundary of the simulation domain is used to force the velocity field back to its value at the inflow boundary, which allows the simulation of the nonperiodic flow using the periodic pseudospectral flow solver. Specifically, let x_{fr} and x_{out} be the x coordinates for the starting location of the fringe zone and the outflow boundary of the simulation domain, respectively. The velocity within the fringe zone $x_{fr} \leq x \leq x_{out}$ is imposed as $\tilde{\mathbf{u}}(x, y, z) = \tilde{\mathbf{u}}(x_{fr}, y, z)[1 - f(x)] + (U_c\mathbf{e}_x)f(x)$, where U_c is the imposed crossflow velocity in the x -direction at the inflow boundary, \mathbf{e}_x is the unit vector in the x -direction, and $f(x) = 0.5 - 0.5 \cos[\pi(x - x_{fr})/(x_{out} - x_{fr})]$ is the fringe function. A similar fringe zone method has been successfully applied in the Fourier-series-based pseudospectral LES

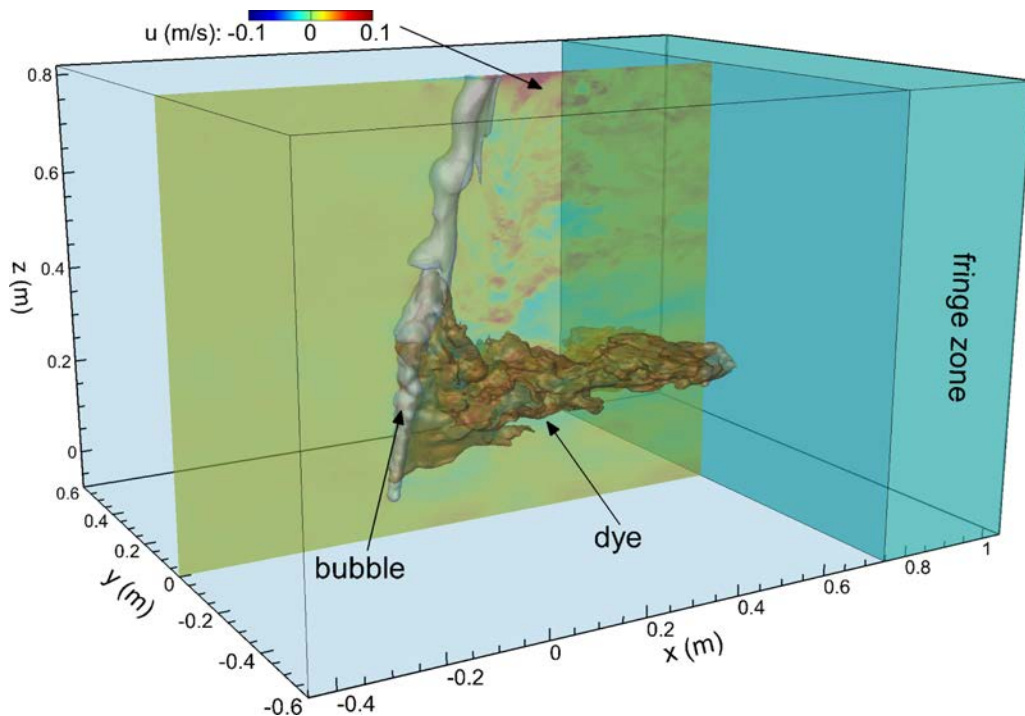


FIG. 3. Three-dimensional instantaneous plume for case W6U2.

model for simulating nonperiodic turbulent flows past trees (see, e.g., Refs. [59,60]) and wind turbines (see, e.g., Refs. [61,62]).

In the simulation, the top boundary of the simulation domain is kept flat, where the free-slip and impermeability conditions ($\partial\tilde{u}/\partial z = \partial\tilde{v}/\partial z = 0$ and $\tilde{w} = 0$) are used for the velocity field. At the top boundary, a no-flux condition ($\partial\tilde{C}_{\text{dye}}/\partial z = 0$) is used for the dye concentration field, and an outflux condition ($\Phi_s = w_r\tilde{C}_b|_{\text{surface}}$) is used to release the gas from the simulation domain when the bubbles reach the top boundary. Similar top surface conditions have been used in Yang *et al.* [14]. The bottom boundary of the simulation domain is set to be flat, where the free-slip and impermeability conditions are applied for the velocity field and the no-flux condition is used for both the bubble and dye concentrations. Recently, the present LES solver with the fringe zone method and similar top and bottom boundary conditions has also been successfully applied to model the dynamics of oil jet in crossflow [35], and good agreement with the data of a towing tank experiment [63] was obtained.

III. CONFIGURATION OF SIMULATION CASES

The physical parameters of the simulations are chosen to be similar to those used in the previously reported laboratory experiments and numerical simulations [14,64]. In all the simulation cases, the computational domain height is set to be $H = 0.9$ m. The air bubbles with density $\rho_b = 1.4$ kg/m³ are released at a total volume release rate of $Q_b = 1.5 \times 10^{-6}$ m³/s from a localized source at 0.08 m above the bottom boundary. This source location mimics the typical laboratory experimental condition in which the plume source is placed at some distance above the bottom of the water tank to avoid significant influence of the bottom boundary on the plume dynamics (see, e.g., Refs. [4,19,63–66]). A similar configuration of plume source location has also been used in other recent LES studies [14,35]. The corresponding kinematic buoyancy flux induced by the bubble

TABLE I. Key parameters for the LES cases: w_r is the dimensional bubble rise velocity; U_c is the dimensional crossflow velocity; B_0 is the bubble source kinematic buoyancy flux; N is the buoyancy frequency of the stratified water; W_N is the dimensionless bubble rise velocity defined by Eq. (1); $h_{p,LES}$ is the mean plume peel heights estimated based on the LES data; $h_{p,0}$ is the mean plume peel height predicted by the empirical formula (12) for plume in stratified water without crossflow; and $h_{s,0}$ is the separation height of the bubble and entrained water predicted by the empirical formula (11) for plume in unstratified water with crossflow.

Case ID	w_r (cm/s)	U_c (cm/s)	B_0 ($\text{m}^4/\text{s}^3; 10^{-5}$)	N (s^{-1})	W_N	$h_{p,LES}$ (m)	$h_{p,0}$ (m)	$h_{s,0}$ (m)
Wr3-Uc05	3	0.5	1.47	0.7	0.53	0.38	0.36	13.06
Wr3-Uc1	3	1	1.47	0.7	0.53	0.37	0.36	7.10
Wr3-Uc2	3	2	1.47	0.7	0.53	0.38	0.36	3.86
Wr6-Uc0	6	0	1.47	0.7	1.06	0.39	0.40	∞
Wr6-Uc05	6	0.5	1.47	0.7	1.06	0.38	0.40	3.02
Wr6-Uc1	6	1	1.47	0.7	1.06	0.38	0.40	1.64
Wr6-Uc2	6	2	1.47	0.7	1.06	0.40	0.40	0.89
Wr12-Uc05	12	0.5	1.47	0.7	2.12	0.39	0.42	0.70
Wr12-Uc1	12	1	1.47	0.7	2.12	0.37	0.42	0.38
Wr12-Uc2	12	2	1.47	0.7	2.12	0.36	0.42	0.21
Wr20-Uc05	20	0.5	1.47	0.7	3.53	0.36	0.31	0.24
Wr20-Uc1	20	1	1.47	0.7	3.53	0.32	0.31	0.13
Wr20-Uc2	20	2	1.47	0.7	3.53	0.33	0.31	0.07

source is $B_0 = gQ_b(\rho_0 - \rho_b)/\rho_0 = 1.47 \times 10^{-5} \text{ m}^4/\text{s}^3$, where $\rho_0 = 1000 \text{ kg}/\text{m}^3$. By setting the origin of the coordinate system to be at the center of the bubble releasing source, the vertical domain ranges from $z = z_{\text{bot}} = -0.08 \text{ m}$ to $z = z_{\text{top}} = 0.82 \text{ m}$. The air bubble source is smeared smoothly using a super Gaussian function over a finite cylindrical volume of $V_s = \pi b_s^2 h$, with a source radius $b_s = 7 \text{ mm}$ and a height $h = 6.25 \text{ mm}$ (i.e., two times of the vertical grid size, which is specified below).

The water in the simulation domain is linearly stratified from $z = -0.08 \text{ m}$ (bottom) to $z = 0.72 \text{ m}$ with a constant density gradient of $\partial\rho/\partial z = -50 \text{ kg}/\text{m}^4$, which corresponds to a buoyancy frequency of $N = \sqrt{-(g/\rho_0)\partial\rho/\partial z} = 0.7 \text{ s}^{-1}$. The top 0.1 m of the simulation domain has a uniform water density of $\rho_0 = 1000 \text{ kg}/\text{m}^3$ to mimic the effect of the surface mixed layer in oceans and lakes. This uniform density layer helps to prevent the plume flow and internal waves from reflecting back to the lower portion of the simulation domain by the top surface to ensure that the observed plume phenomena are governed by the interaction between the bubble-driven plume and the stratified crossflow. A similar setup of water stratification with a top layer of uniform water density has also been used in previous experimental and numerical studies of bubble-driven plumes (see, e.g., Refs. [14,64]).

The passive scalar dye is released into the center of the plume at a height of 3.75 cm (i.e., 12 vertical grid sizes) above the air bubble source with a mass release rate of $Q_{\text{dye}} = 5 \times 10^{-3} \text{ mg}/\text{s}$. This slight upward shift of the dye release source relative to the bubble source results in the dye being injected at a location where the plume has gained sufficient vertical momentum to carry the dye. If the dye was released at the same location as the bubbles, a considerable fraction of the dye would be directly carried away by the crossflow due to the weak upward plume velocity in the vicinity of the bubble source. This effect would not only reduce the amount of dye available for tracing the plume dynamics, but also contaminate the lower portion of the dye concentration field generated by the plume dynamics.

As listed in Table I, four different bubble rise velocities are considered in this study: $w_r = 3, 6, 12, \text{ and } 20 \text{ cm}/\text{s}$. These rise velocities correspond to the equivalent bubble diameters of $d = 0.31, 0.53, 1.01, \text{ and } 2.02 \text{ mm}$, respectively, based on the empirical parametrization shown in Eqs. (8) and

(9). It should be noted that the present LES model uses w_r as the input parameter in Eq. (7). The corresponding bubble equivalent diameters d may be slightly different if a different parametrization of $w_r(d)$ is used for the estimation, which does not affect the simulation results since d is not directly used as an input parameter in the LES model. The corresponding values of the dimensionless bubble rise velocity based on Eq. (1) for the four w_r are $W_N = 0.53, 1.06, 2.12,$ and 3.53 , respectively. These conditions cover the three representative plume categories according to the plume classification identified in the previous experimental studies [9,11,19]: (1) the cases with $W_N = 0.53$ and 1.06 fall into the Type 1* regime, in which the distinct peeling event occurs and the bubble column above it is dispersed horizontally due to the radial motion of the peeling flow; (2) the case with $W_N = 2.12$ is in the Type 2 regime, in which the distinct peeling event occurs but the bubble column remain narrow above it; (3) the case with $W_N = 3.53$ is in the Type 3 regime, in which the peeling events become unstable and occur continuously along the rising plume.

Note that due to the additional effect of the crossflow, the actual plume structures for the four W_N cases considered in this study are expected to be different from the schematics shown in Figs. 1(b)–1(d) that are for the plumes without crossflow. For each bubble condition, three different crossflow velocities are investigated: $U_c = 0.5, 1,$ and 2 cm/s. In addition, a reference case without crossflow is also considered for $w_r = 6$ cm/s. Each simulation case is named in terms of the corresponding bubble rise velocity and crossflow velocity (see Table I). For example, the case with $w_r = 3$ cm/s and $U_c = 0.5$ cm/s is referred to as case Wr3-Uc05. These relatively weak crossflow velocities are chosen to ensure that the crossflow does not force the bubbles and the entrained water stream in the plume to separate too early so that the bubble/water mixed plume can have sufficient interaction with the stratified water to generate the peeling and intrusion. For the Type 1* and Type 2 plumes that have a distinct peeling process, the strength of the crossflow may be estimated based on the critical separation height $h_{s,0}$ and the plume peel height $h_{p,0}$. Here, $h_{s,0}$ denotes the bubble/water separation height in the crossflow without stratification, which can be estimated based on the empirical parametrization from Socolofsky and Adams [19],

$$h_{s,0} = \frac{5.1B_0}{(U_c w_r^{2.4})^{0.88}}, \quad (11)$$

and $h_{p,0}$ denotes the peel height for plume in stratified water without crossflow estimated based on the empirical parametrization from Socolofsky and Adams [9],

$$h_{p,0} = 5.2 \left(\frac{B_0}{N^3} \right)^{1/4} \exp \left\{ -\frac{1}{10.1} \left[\frac{w_r}{(B_0 N)^{1/4}} - 1.8 \right]^2 \right\}. \quad (12)$$

Socolofsky and Adams [19] and Socolofsky *et al.* [10] suggested that the plume structure is dominated by the crossflow effect if $h_{s,0} < h_{p,0}$ and by the stratification effect if $h_{s,0} > h_{p,0}$. As shown in Table I, the condition $h_{s,0} > h_{p,0}$ is satisfied for the cases with $w_r = 3$ and 6 cm/s, suggesting that the stratification effect dominates in these cases. On the other hand, for the cases with $w_r = 12$ and 20 cm/s, the estimated $h_{s,0}$ are comparable to or smaller than $h_{p,0}$, suggesting that the crossflow is expected to generate more significant impact on the plume dynamics. Overall, the three crossflow conditions considered in the present study fall into the weak crossflow category [19]. As shown by the simulation results in Sec. IV, although the crossflow can tilt the plume, it is not strong enough to force the bubble/water separation and prevent the plume peeling process from occurring. In all the reported cases, the bubble-driven plume interacts with the stratified water to create the peeling process and form the rising/falling double plume structure.

As illustrated in Fig. 3, for the simulation cases with crossflow, the horizontal domain dimensions are set to be $L_x = 1.5$ m and $L_y = 1.2$ m for the x - and y -directions, respectively. The simulation domain is discretized using $N_x \times N_y \times N_z = 320 \times 256 \times 289$ grid points, with even grid spacing in each direction. In the x -direction, a uniform streamwise velocity U_c is imposed at the inflow boundary at 0.45 m upstream from the bubble source. The last 0.3 m of the streamwise domain is set to be the fringe zone for imposing the outflow condition, as explained in Sec. II. For case

Wr6-Uc0 without the crossflow, the simulation domain is set to be $(L_x, L_y, H) = (1.5, 1.5, 0.9)$ m, which has equal dimensions in the x - and y -directions. No fringe zone is used in case Wr6-Uc0. To have identical grid resolution as other simulation cases with the crossflow, the simulation domain in case Wr6-Uc0 is discretized using $N_x \times N_y \times N_z = 320 \times 320 \times 289$ grid points. The bubble source in case Wr6-Uc0 is located at the center of the horizontal domain at the same depth as in other simulation cases with crossflow. All the 13 simulation cases included in this study have the same grid resolution of $(\Delta x, \Delta y, \Delta z) = (4.6875, 4.6875, 3.125)$ mm. Recently, Peng *et al.* [34] simulated the plume dynamics in deep stratified water without crossflow. They performed grid convergence tests and showed that the current LES solver can produce consistent simulation results with various grid resolutions. In the present study, additional grid convergence tests were performed for the simulation of plume in crossflow (see Appendix B), and the results show that the grid resolution used in the present study is sufficient for capturing the correct plume flow physics.

IV. RESULTS

A. Instantaneous plume characteristics

Figure 4 shows the instantaneous plume of the reference case Wr6-Uc0. The basic dynamics of the bubble-driven plume in stably stratified water can be seen from the scalar and velocity fields of this case. Due to their smaller density than the surrounding water, the air bubbles rise towards the water surface along a vertical column. The bubble-induced buoyancy also drives the water around the bubble source to rise together as a plume of water/bubble mixture. The turbulent eddies at the edge of the plume cause entrainment of surrounding water into the plume when it rises through the stably stratified water, and lift the higher density water to higher elevations where the ambient water has a lower density. This density difference results in a downward force to act against the buoyancy induced by the bubbles, which eventually causes the water flow in the plume to lose the upward momentum and detrain from the bubble column at the peel height around $z = 0.4$ m. Without the crossflow, the bubble/water mixed plume rises vertically and the detrained water forms an annular plume to fall along the outside of the rising plume [4,11,14]. As shown later in Sec. IV B, the inner/outer double plume structure is nearly axisymmetric about the vertical axis at the center of the plume. The detrained water falls as a downward plume to the neutral buoyancy level and forms an horizontal intrusion layer at around $z = 0.2$ m.

Differently, in case Wr6-Uc05 with the weak crossflow of $U_c = 0.5$ cm/s (Fig. 5), the bubble/water mixed rising plume is slightly tilted towards the positive x -direction, and the plume velocity and dye concentration fields are no longer axisymmetric about the center line of the rising plume. In particular, the horizontal peeling flow [Fig. 5(c)] and the subsequent falling plume [Fig. 5(d)] bias towards the downstream direction of the crossflow, causing the intrusion layer to form mainly towards the positive x -direction with a weak upstream intrusion layer extended only up to $x = -0.1$ m [Fig. 5(b)]. If the crossflow becomes faster, as shown in Fig. 6 for case Wr6-Uc2, the bubble plume further tilts towards the downstream direction of the crossflow [Fig. 6(a)]. With the $U_c = 2$ cm/s crossflow velocity, the intrusion towards the upstream direction is completely suppressed [Fig. 6(b)]. In case Wr6-Uc2, the detrained water forms a stronger downward plume than that in case Wr6-Uc05, as indicated by the much larger region of downward velocity at around $(x, z) = (0.15, 0.3)$ m shown in Fig. 6(d) than the smaller region of downward velocity at around $(x, z) = (0.07, 0.25)$ m shown in Fig. 5(d). This is because the faster crossflow tilts the bubble/water plume sufficiently away from being vertical, allowing the downward plume to fall on the downstream side of the rising plume with less contact. More quantitative comparison of the downward plume velocity under different crossflow velocities is given in Sec. IV B based on the time averaged plume. Compared with case Wr6-Uc05, the intrusion layer in case Wr6-Uc2 expands more towards lower elevation and has lower local dye concentration [Fig. 6(b) versus Fig. 5(b)]. Further analysis on the dye flux from the plume into the intrusion layer is presented in Sec. IV C. The

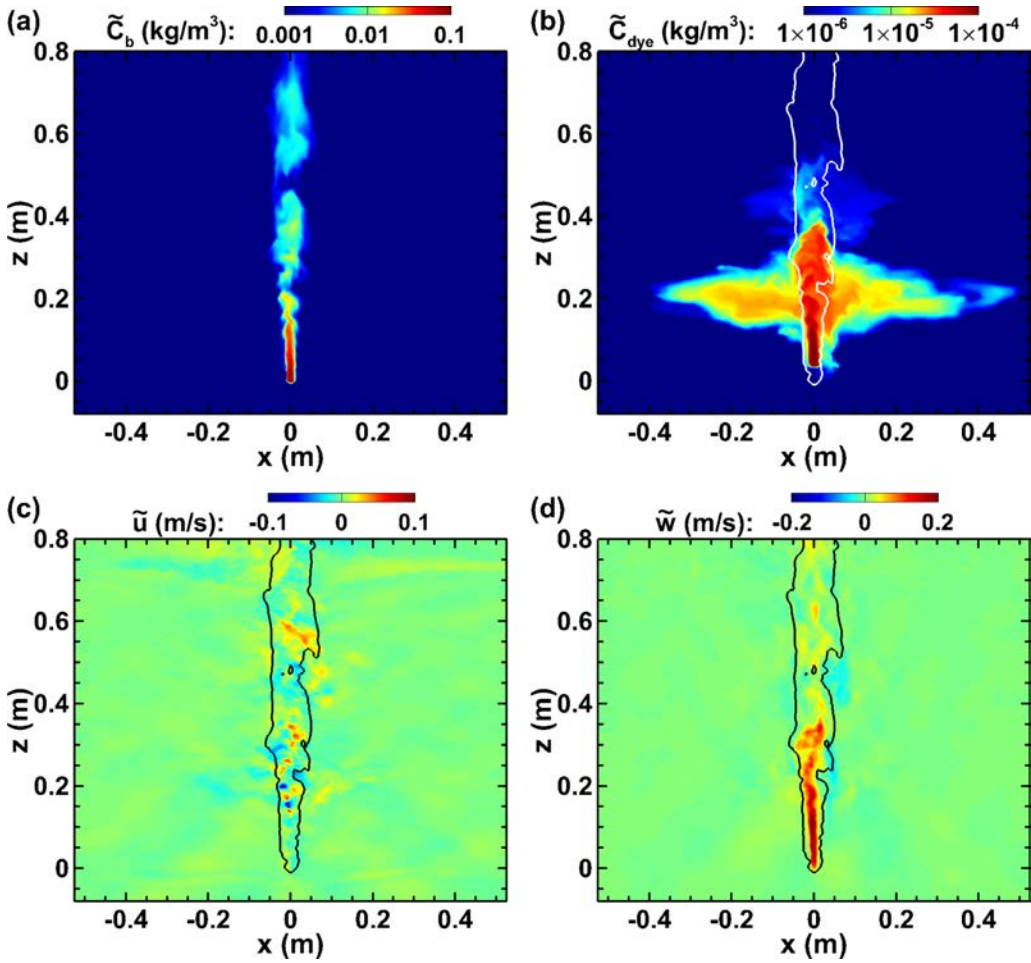


FIG. 4. Instantaneous plume velocity and scalar fields on the (x, z) -plane across the source location for case Wr6-Uc0 ($w_r = 6$ cm/s, $U_c = 0$ cm/s): (a) bubble concentration \tilde{C}_b ; (b) dye concentration \tilde{C}_{dye} ; (c) streamwise velocity \tilde{u} ; (d) vertical velocity \tilde{w} . In (b)–(d) the solid lines are the isolines of $\tilde{C}_b = 0.001$ kg/m³, which are used to indicate the shape and location of the bubble column.

bubble column in case Wr6-Uc2 also shows a clear increase of tilt angle at the peel height (around $z = 0.4$ m) as the peeling process expands the bubble column and reduces the bubble concentration, resulting in smaller upward velocity for the plume above the peel height [Fig. 6(d)].

Changing the bubble rise velocity also affects the dynamics of the plume in the crossflow. Figures 7 and 8 show the instantaneous plumes for cases Wr20-Uc05 and Wr20-Uc2, respectively. Compared with the cases with smaller bubble rise velocity of $w_r = 6$ cm/s, the bubble columns in the cases with $w_r = 20$ cm/s exhibit less horizontal dispersion and smaller tilt angle because of the stronger buoyancy of the larger bubbles. Note that the cases with $w_r = 20$ cm/s have the same dimensionless rise velocity of $W_N = 3.53$, which falls into the plume category of Type-3 featuring unstable continuous peeling process along the edge of the rising plume [9, 11, 19]. The combination of the unstable peeling in cases Wr20-Uc05 and Wr20-Uc2 with the crossflow causes a considerable amount of dye to leak from the plume at a wide range of heights, resulting in more vertical spreading of the dye intrusion layer than that in the cases with $w_r = 6$ cm/s [see Figs. 7(b) and 8(b) versus Figs. 5(b) and 6(b)]. The comparison between cases Wr20-Uc05 and Wr20-Uc2 also shows that the

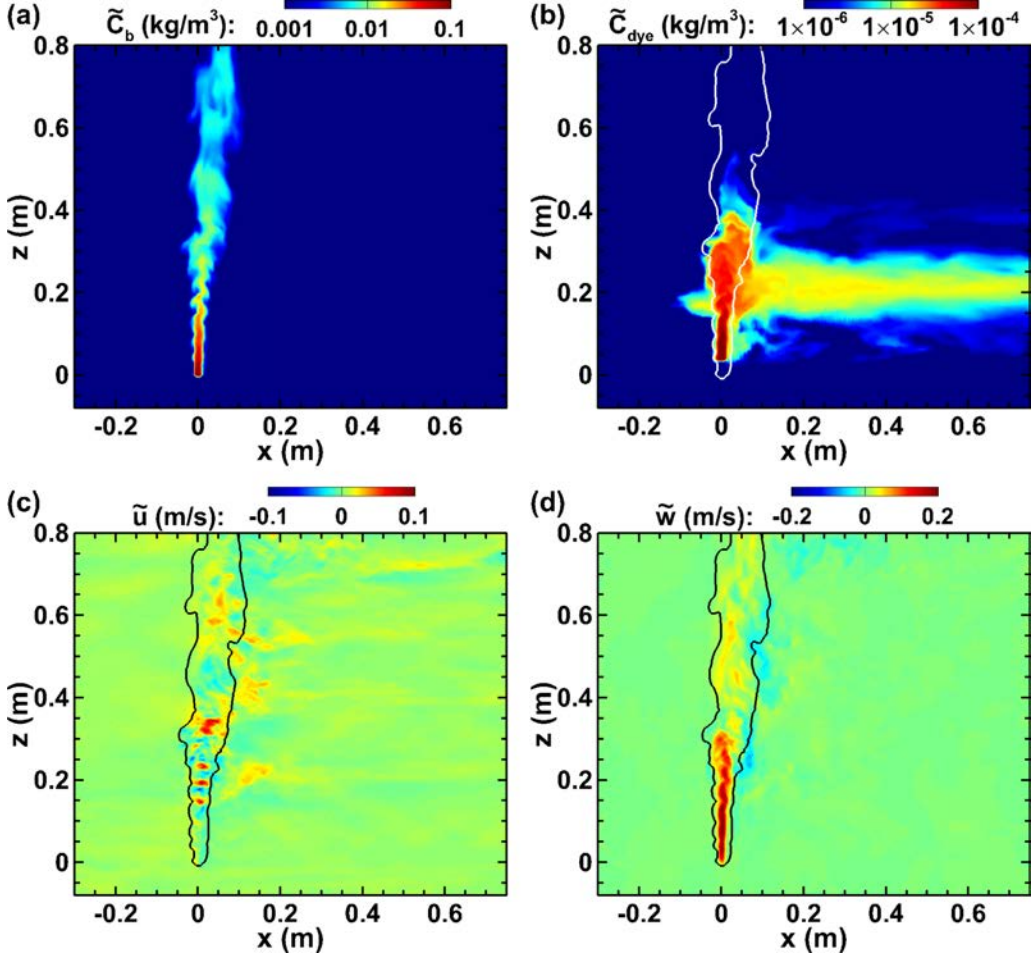


FIG. 5. Instantaneous plume velocity and scalar fields on the (x, z) -plane across the source location for case Wr6-Uc05 ($w_r = 6 \text{ cm/s}$, $U_c = 0.5 \text{ cm/s}$): (a) bubble concentration \tilde{C}_b ; (b) dye concentration \tilde{C}_{dye} ; (c) stream-wise velocity \tilde{u} ; (d) vertical velocity \tilde{w} . In (b)–(d) the solid lines are the isolines of $\tilde{C}_b = 0.001 \text{ kg/m}^3$, which are used to indicate the shape and location of the bubble column.

increase of crossflow velocity causes the plume in case Wr20-Uc2 to be further tilted towards the positive x -direction, resulting in a stronger falling plume on the downstream side of the rising plume [Figs. 7(d) and 8(d)] that pushes the upper edge of the intrusion layer to a lower elevation than that in case Wr20-Uc05 [Figs. 7(b) and 8(b)].

B. Mean plume statistics

The instantaneous plume field exhibits considerable fluctuations in velocities and scalar concentrations due to the turbulence effect of the plume flow as well as the unsteadiness of the peeling process [64]. Here the time average is performed to obtain the mean plume field, which helps to illustrate the effect of crossflow on the averaged plume structure and material transport. Hereinafter, the time average of a LES-resolved physical quantity \tilde{f} is denoted as \bar{f} . For all the reported cases, the bubbles were released at $t = 0 \text{ s}$ and the simulations were performed till the plume flow and dye concentration fields have reached statistically steady state. After that, the instantaneous snapshots of

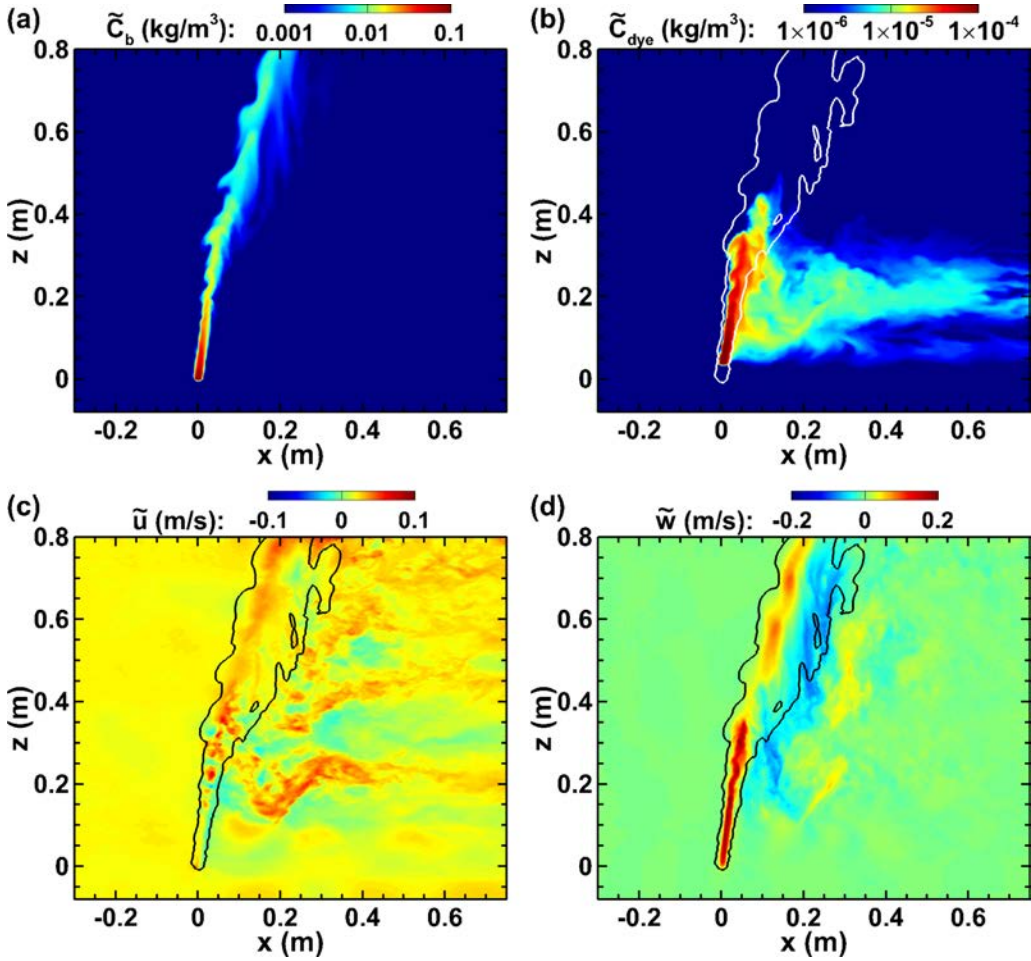


FIG. 6. Instantaneous plume velocity and scalar fields on the (x, z) -plane across the source location for case Wr6-Uc2 ($w_r = 6$ cm/s, $U_c = 2$ cm/s): (a) bubble concentration \tilde{C}_b ; (b) dye concentration \tilde{C}_{dye} ; (c) streamwise velocity \tilde{u} ; (d) vertical velocity \tilde{w} . In (b)–(d) the solid lines are the isolines of $\tilde{C}_b = 0.001$ kg/m³, which are used to indicate the shape and location of the bubble column.

the entire three-dimensional simulation domain were sampled from $t = 80$ to 200 s with a fixed time interval of 0.25 s between each sample. Altogether, a total number of 480 instantaneous snapshots of the full simulation domain were used for time averaging in each case.

Figure 9 shows the time-averaged dye concentration for the plume of $w_r = 6$ cm/s with four different crossflow velocities of $U_c = 0, 0.5, 1,$ and 2 cm/s. Following Seol *et al.* [64], the mean peel height is evaluated based on the maximum elevation of the 5% threshold contour line of the maximum time-averaged dye concentration (e.g., the dashed lines in Fig. 9). The mean peel heights evaluated based on this approach are listed in Table 1 as $h_{p,LES}$. For case Wr6-Uc0 [Fig. 9(a)], without the presence of crossflow, the time-averaged dye concentration is nearly axisymmetric about the plume center axis. The spatial distribution of the dye concentration shows that a primary peeling event occurs at about $z = 0.4$ m, causing most of the initially entrained water to detrain from the rising plume (as indicated by the much lower dye concentration further above) and fall to the neutral buoyancy level to form the thin intrusion layer at around $z = 0.2$ m. This high peel fraction associated with the primary peeling event shown by the present LES result is consistent

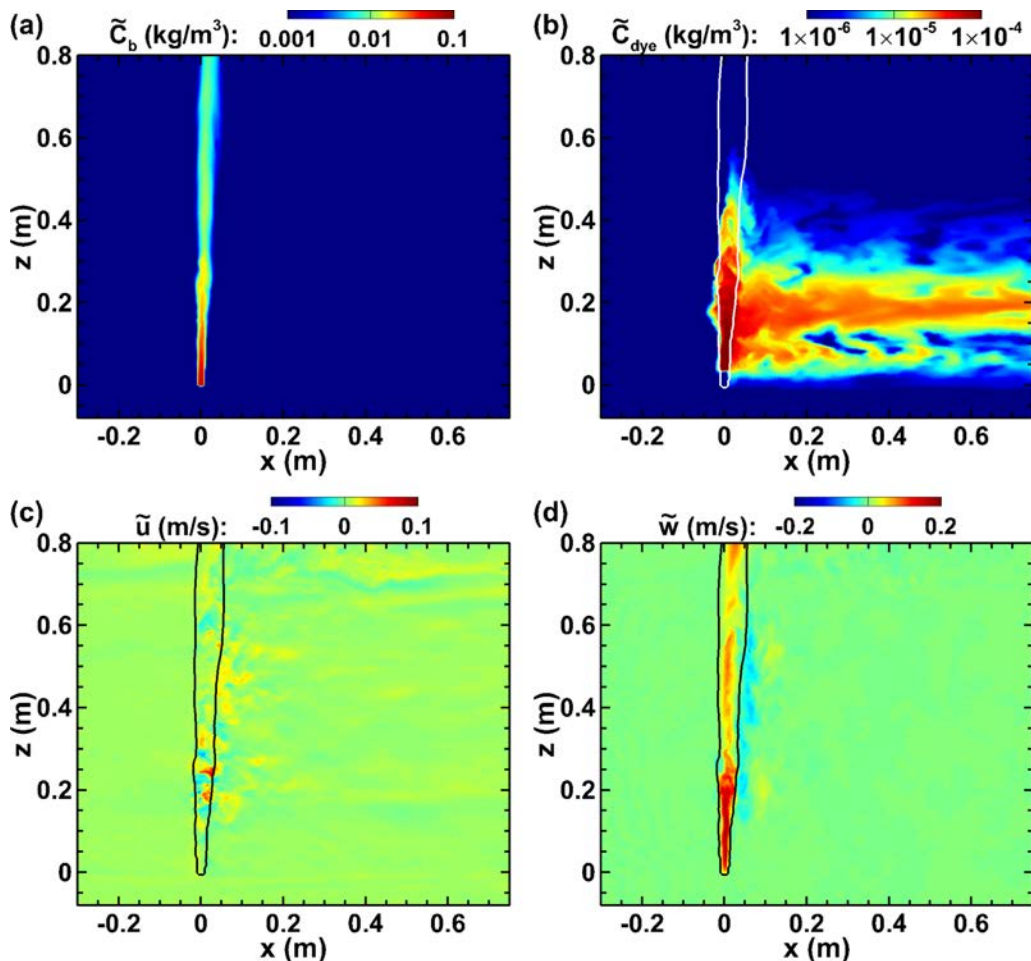


FIG. 7. Instantaneous plume velocity and scalar fields on the (x, z) -plane across the source for case Wr20-Uc05 ($w_r = 20$ cm/s, $U_c = 0.5$ cm/s): (a) bubble concentration C_b ; (b) dye concentration C_{dye} ; (c) streamwise velocity u ; (d) vertical velocity w . In (b)–(d) the solid lines are the isolines of $C_b = 0.001$ kg/m³, which are used to indicate the shape and location of the bubble column.

with the experimental observation reported in Socolofsky and Adams [9] and Socolofsky *et al.* [10]. Only a very small fraction of entrained water can escape from the primary peeling event and continue to rise upwards with the bubble plume. Further upwards, the bubble plume repeats the water entrainment/peel process in the region at $0.4 \lesssim z \lesssim 0.6$ m and forms a secondary intrusion layer at about $z = 0.4$ m, where the small fraction of the initially entrained water (from the ambient water below the primary peel height) that survived the primary peeling event gets fully trapped. A similar secondary intrusion layer above the primary peel height has also been observed in previous experimental and numerical studies [9,10,14,15].

For case Wr6-Uc05 [Fig. 9(b)], the weak crossflow of $U_c = 0.5$ m/s significantly suppresses the upstream intrusion (i.e., towards the negative x -direction) and slightly increases the vertical expansion of the primary intrusion layer at around $z = 0.2$ m on the downstream side of the plume. The trace of the secondary peeling/intrusion process can be seen from the horizontal intrusion of the dye at around $z = 0.4$ m, which has much lower dye concentration than that in the main intrusion layer. As the crossflow velocity further increases, in cases Wr6-Uc1 [Fig. 9(c)] and

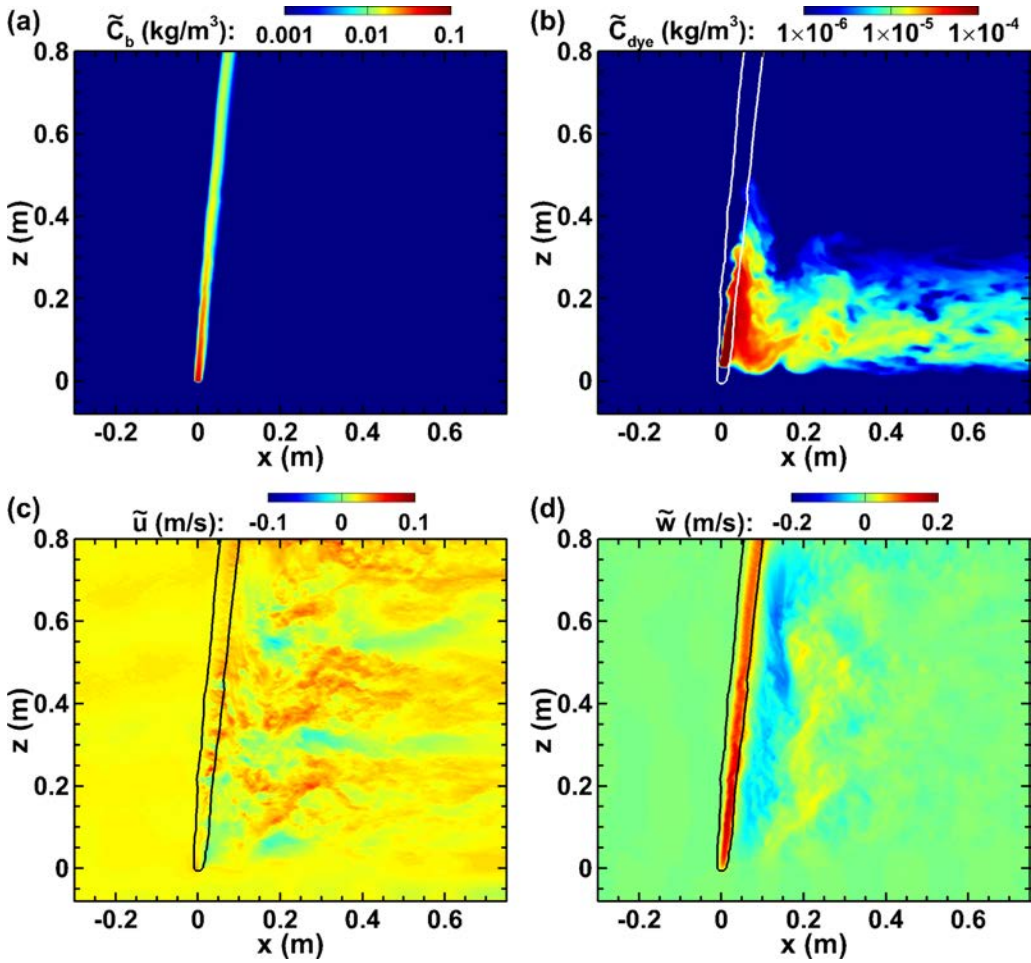


FIG. 8. Instantaneous plume velocity and scalar fields on the (x, z) -plane across the source for case Wr20-Uc2 ($w_r = 20$ cm/s, $U_c = 2$ cm/s): (a) bubble concentration \tilde{C}_b ; (b) dye concentration \tilde{C}_{dye} ; (c) streamwise velocity \tilde{u} ; (d) vertical velocity \tilde{w} . In (b)–(d) the solid lines are the isolines of $\tilde{C}_b = 0.001$ kg/m^3 , which are used to indicate the shape and location of the bubble column.

Wr6-Uc2 [Fig. 9(d)], nearly all the initially entrained water detains from the rising plume at the peel height around $z = 0.4$ m, and no clear sign of secondary peeling/intrusion process is observed further above. Moreover, a small fraction of water leaks directly from the bottom stem of the plume due to the crossflow in cases Wr06-Uc1 and Wr06-Uc2. Unlike the water that escapes from the rising plume at the peel height, the water leaked from the stem of the plume does not experience considerable mixing with the lower density ambient water at higher elevation. Thus this stream of water with higher density (with respect to the water in the primary intrusion layer) forms a secondary intrusion layer at around $z = 0.08$ m that extends directly from the bottom stem of the rising plume.

Figure 10 compares the time-averaged dye concentration for the plumes of $w_r = 3, 6, 12,$ and 20 cm/s with the same crossflow velocity of $U_c = 2$ cm/s. Similar to the observation from the instantaneous plume fields shown in Figs. 6 and 8, the time-averaged plumes shown in Fig. 10 also exhibit different characteristics under the same crossflow condition when the bubble rise velocity is changed. In particular, the mean bubble columns in cases Wr3-Uc2 and Wr6-Uc2 are clearly affected by both the peeling process and the crossflow, exhibiting an expansion of the bubble column

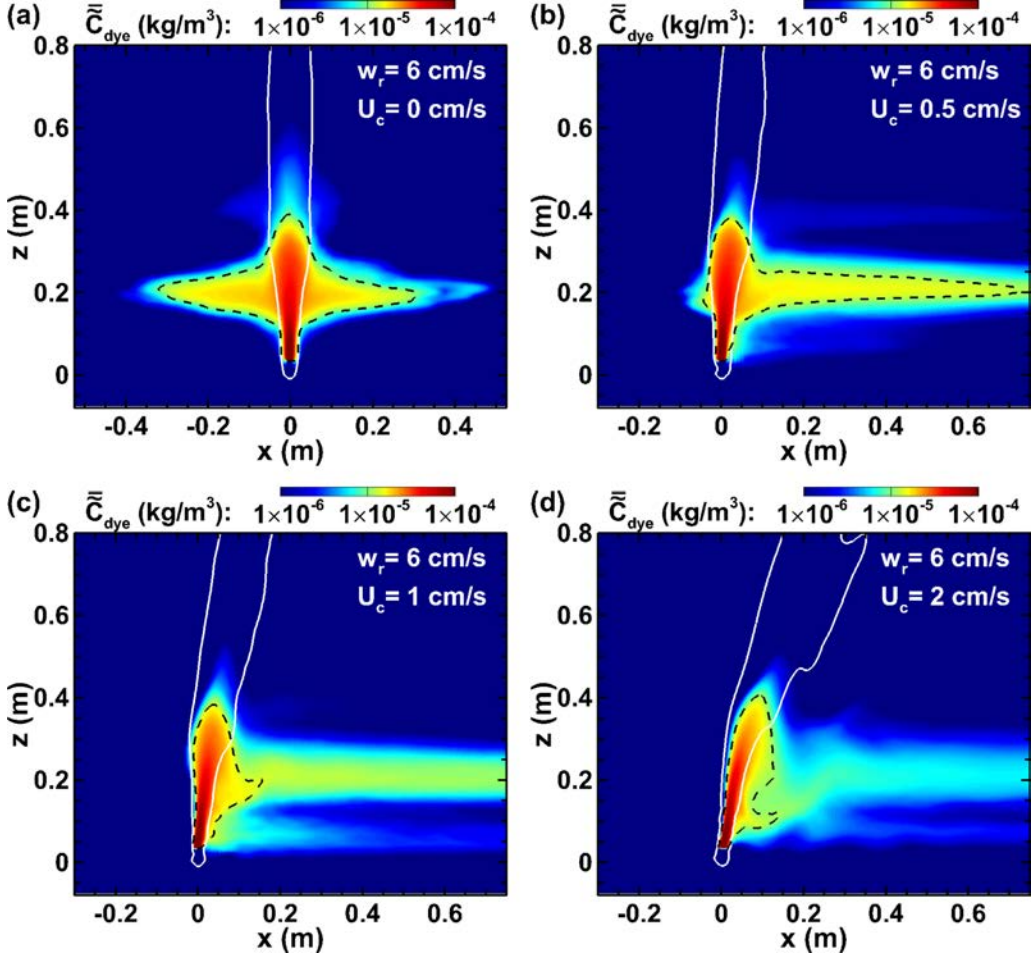


FIG. 9. Time-averaged plumes on the (x, z) -plane across the source for $w_r = 6$ cm/s: (a) Wr6-Uc0; (b) Wr6-Uc05; (c) Wr6-Uc1; (d) Wr6-Uc2. The color contours are for the time-averaged dye concentration; the solid lines are the isolines for the time-averaged bubble mass concentration of 0.001 kg/m³, which are used to indicate the location and shape of the bubble column, and the dashed lines are the isolines of $5\% \max\{\bar{C}_{\text{dye}}\}$, which are used to define the mean peel height.

width and an increase of its tilt angle above the peel height at about $z = 0.4$ m. Some bubbles in case Wr3-Uc2 are also pushed down quite a bit by the falling plume from the peeling event, as indicated by the convex bubble concentration isoline shown in Fig. 10(a) at around $(x, z) = (0.2, 0.25)$ m. In cases Wr3-Uc2 and Wr6-Uc2, most of the dye is carried into the primary intrusion layer at around $z = 0.2$ m, but the secondary intrusion layer at the lower elevation around $z = 0.08$ m is still noticeable. As the bubble rise velocity increases to $w_r = 12$ cm/s in case Wr12-Uc2 [Fig. 10(c)], the primary peeling process occurs at a lower elevation near $z = 0.3$ m, and the narrow rising plume also releases water and dye continuously into the crossflow at low elevation. As a result, the dye concentration in the secondary intrusion layer at around $z = 0.08$ m reaches a comparable level as that in the primary intrusion layer at around $z = 0.2$ m. In case Wr20-Uc2 [Fig. 10(d)], the unstable and continuous peeling processes completely dominate and the dye is transported by the crossflow into a continuous intrusion layer ranging from about $z = 0.02$ to 0.3 m, with higher dye concentration near the lower elevation. More discussion on the dye fluxes due to mean plume flow

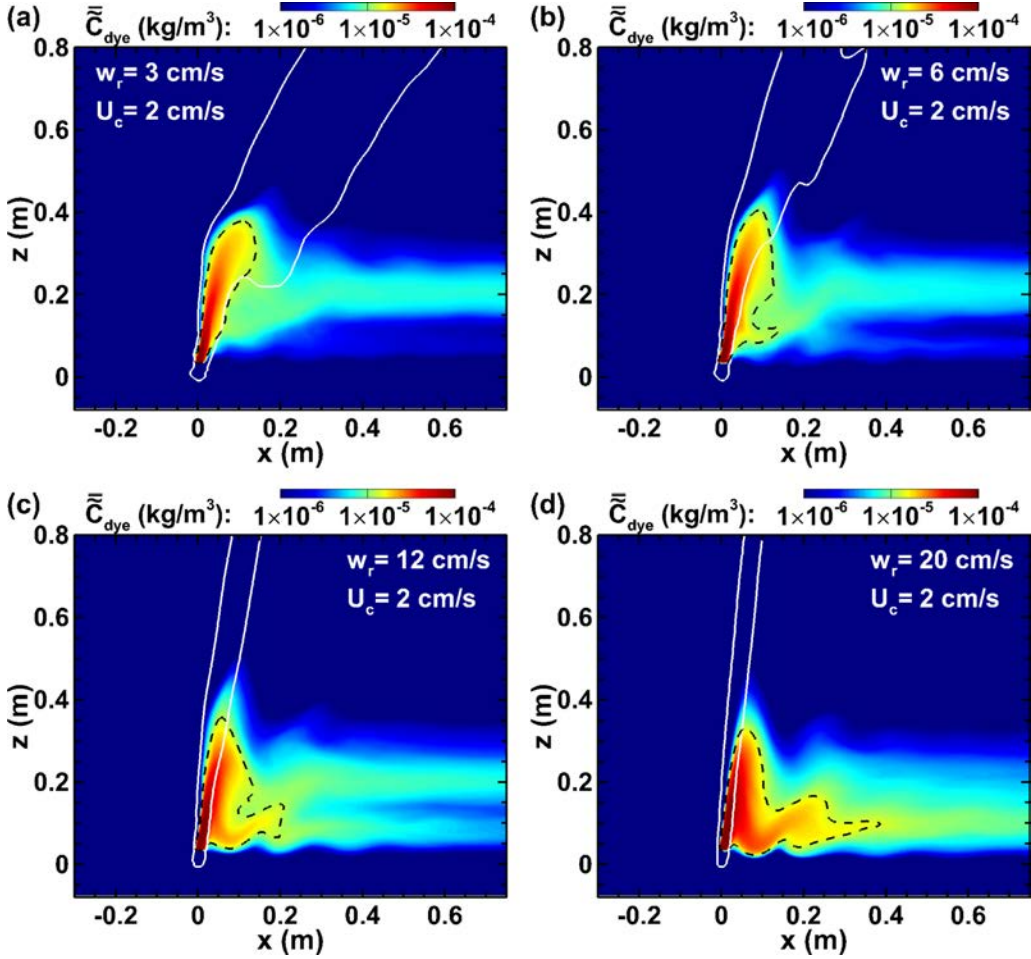


FIG. 10. Time-averaged plumes on the (x, z) -plane across the source for $U_c = 2$ cm/s: (a) Wr3-Uc2; (b) Wr6-Uc2; (c) Wr12-Uc2; (d) Wr20-Uc2. The color contours are for the time-averaged dye concentration; the solid lines are the isolines for the time-averaged bubble mass concentration of 0.001 kg/m³, which are used to indicate the location and shape of the bubble column, and the dashed lines are the isolines of $5\% \max\{\bar{C}_{\text{dye}}\}$, which are used to define the mean peel height.

and turbulent fluctuation is presented in Sec. IV C to explain the formation of the dye concentration field presented in this section.

The presence of crossflow can break the axisymmetry of the bubble-driven plume, causing the flow and dye concentration fields to have more complex three-dimensional (3D) features. To illustrate these 3D features of the time-averaged plume structure, in Fig. 11 the isosurfaces of the flow vertical velocity and dye concentration of the time-averaged plumes are plotted together. The corresponding two-dimensional (2D) contours of the averaged vertical velocity \bar{w} on the (x, z) -plane at $y = 0$ m and on the (x, y) -plane at $z = 0.25$ m are shown in Figs. 12 and 13, respectively. Figure 11(a) shows the 3D mean plume structure for case Wr06-Uc0. Without the crossflow, the overall mean plume structure in case Wr06-Uc0 appears to be quite symmetric about the central axis of the plume, including the straight rising plume (indicated by the red isosurfaces of $\bar{w} = 1.5$ cm/s), the annular falling plume (indicated by the blue isosurfaces of $\bar{w} = -1.5$ cm/s), and the pancake-shaped intrusion layer (indicated by the brown isosurfaces of $\bar{C}_{\text{dye}} = 4$ mg/m³). Without the effect

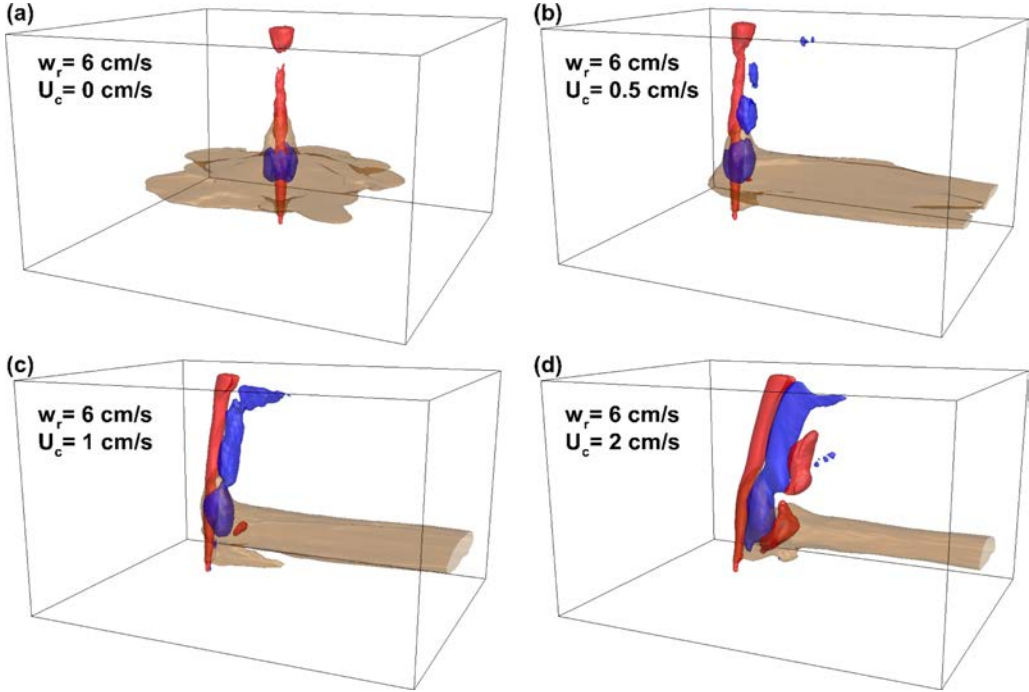


FIG. 11. Time-averaged 3D plumes for $W_r = 6$ cm/s: (a) Wr6-Uc0; (b) Wr6-Uc05; (c) Wr6-Uc1; (d) Wr6-Uc2. The red isosurfaces are for the mean vertical velocity $\bar{w} = 1.5$ cm/s, the blue isosurfaces are for the mean vertical velocity $\bar{w} = -1.5$ cm/s, and the brown isosurfaces are for $\bar{C}_{\text{dye}} = 4$ mg/m³.

of the crossflow, in case Wr06-Uc0 the falling plume formed from the peeling event distributes smoothly in an annular region surrounding the rising plume [Figs. 12(a) and 13(a)]. This annular falling plume interacts with both the inner rising plume and the ambient quiescent water surrounding it, resulting in small downward velocity in case Wr06-Uc0 (i.e., with a peak of $\bar{w} \sim -0.02$ m/s).

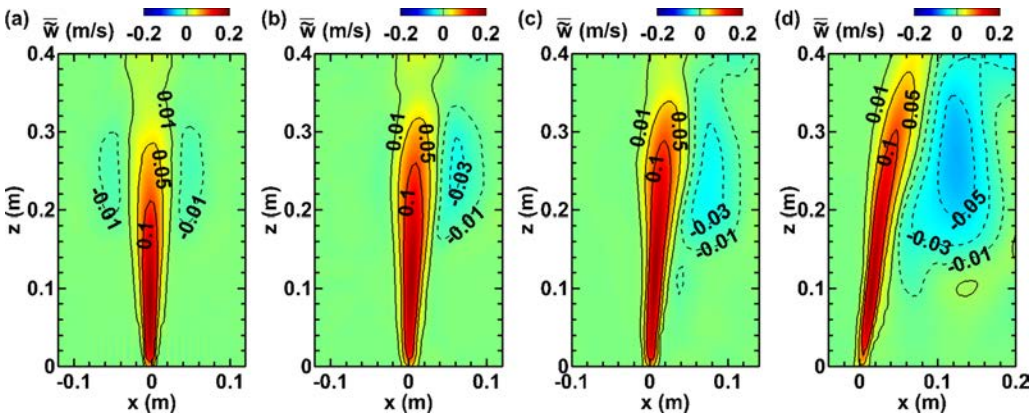


FIG. 12. Time-averaged vertical velocity \bar{w} on the (x, z) -plane at $y = 0$ m for cases with $w_r = 6$ cm/s: (a) Wr6-Uc0; (b) Wr6-Uc05; (c) Wr6-Uc1; (d) Wr6-Uc2. Several representative contour lines of \bar{w} are plotted on top of the smooth 2D color plot, among which the solid lines are for $\bar{w} > 0$ and the dashed lines are for $\bar{w} < 0$.

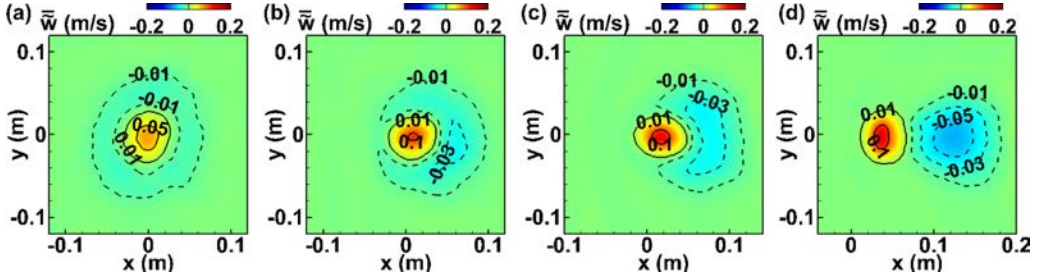


FIG. 13. Time-averaged vertical velocity \bar{w} on the (x, y) -plane at $z = 0.25$ m for cases with $w_r = 6$ cm/s: (a) Wr6-Uc0; (b) Wr6-Uc05; (c) Wr6-Uc1; (d) Wr6-Uc2. Several representative contour lines of \bar{w} are plotted on top of the smooth 2D color plot, among which the solid lines are for $\bar{w} > 0$ and the dashed lines are for $\bar{w} < 0$.

Note that the time-averaged plume shown in Fig. 11(a) is not perfectly axisymmetric. This is as expected because the instantaneous plume snapshots for time average are sampled from only one LES run. Assemble averaging using additional independent instantaneous samples of the turbulent plume field is needed, which can be obtained by performing separate LES runs with a different small disturbance added into the initial condition of the LES. Moreover, the box shape of the computational domain in case Wr06-Uc0 also makes it difficult to obtain a perfect axisymmetric plume. Nevertheless, the simulation result from case Wr06-Uc0 can still serve as a reference to help illustrate the effect of crossflow on the 3D plume characteristics.

Figures 11(b)–11(d) show the time-averaged 3D plume for $w_r = 6$ cm/s under the three different crossflow conditions. As the crossflow velocity increases, the falling plume shifts more towards the downstream side (with respect to the crossflow) of the rising plume, causing the falling plume to no longer surround the rising plume. This downstream shift of the falling plume can also be seen from the 2D plots shown in Figs. 12(b)–12(d) and 13(b)–13(d). In particular, the falling plumes in cases Wr06-Uc05 and Wr06-Uc1 form a semiannular region around the downstream side of the rising plume, while the falling plume in case Wr06-Uc2 has a round shape and much less contact area with the rising plume than those in the other three cases. This reduced contact with increasing U_c causes the magnitude of the vertical flow velocity in both the rising and falling plumes to become greater, as indicated by the increase of volumes enclosed by the isosurfaces of $\bar{w} = \pm 1.5$ m/s shown in Figs. 11(b)–11(d) [also see the 2D contours of \bar{w} shown in Figs. 12(b)–12(d) and 13(b)–13(d)]. Note that in case Wr06-Uc2 [Fig. 11(d)], the high vertical velocity in the falling plume causes it to overshoot, resulting in another rising flow on the downstream side of the falling plume to bring the water back to the neutral buoyancy elevation. The shape of the intrusion layer also exhibits significant variation as the crossflow velocity increases. In case Wr06-Uc05 with $U_c = 0.5$ cm/s [Fig. 11(b)], the intrusion layer (indicated by the brown-colored isosurfaces of dye concentration) is narrow in the vertical direction and wide in the spanwise direction. As the crossflow velocity further increases, the vertical expansion of the intrusion layer further increases while the spanwise width decreases, confining the intrusion of water and dye into a narrow tube-shaped region [Figs. 11(c) and 11(d)].

The rising plume interacts with the ambient water and falling plume via the lateral turbulent flux of the vertical momentum, which consists of two components in LES: the unresolved SGS flux $\tau_{13}^d = -\nu_{\text{sgs}}(\partial\tilde{w}/\partial x + \partial\tilde{u}/\partial z)$ and the resolved turbulent flux $u'w'$. Here $u' = \tilde{u} - \bar{u}$ and $w' = \tilde{w} - \bar{w}$ are the turbulent fluctuations of the resolved velocities \tilde{u} and \tilde{w} , respectively. Figures 14 and 15 show the contours of the time-averaged SGS momentum flux $\overline{\tau_{13}^d}$ and the resolved turbulent momentum flux $\overline{u'w'}$ for the cases with $w_r = 6$ cm/s under four different crossflow conditions, respectively. In all the four cases, $\overline{\tau_{13}^d}$ dominates in the stem region of the rising plume (Fig. 14), resulting in the initial lateral expansion of the plume width when it rises through the ambient water. Towards the peel

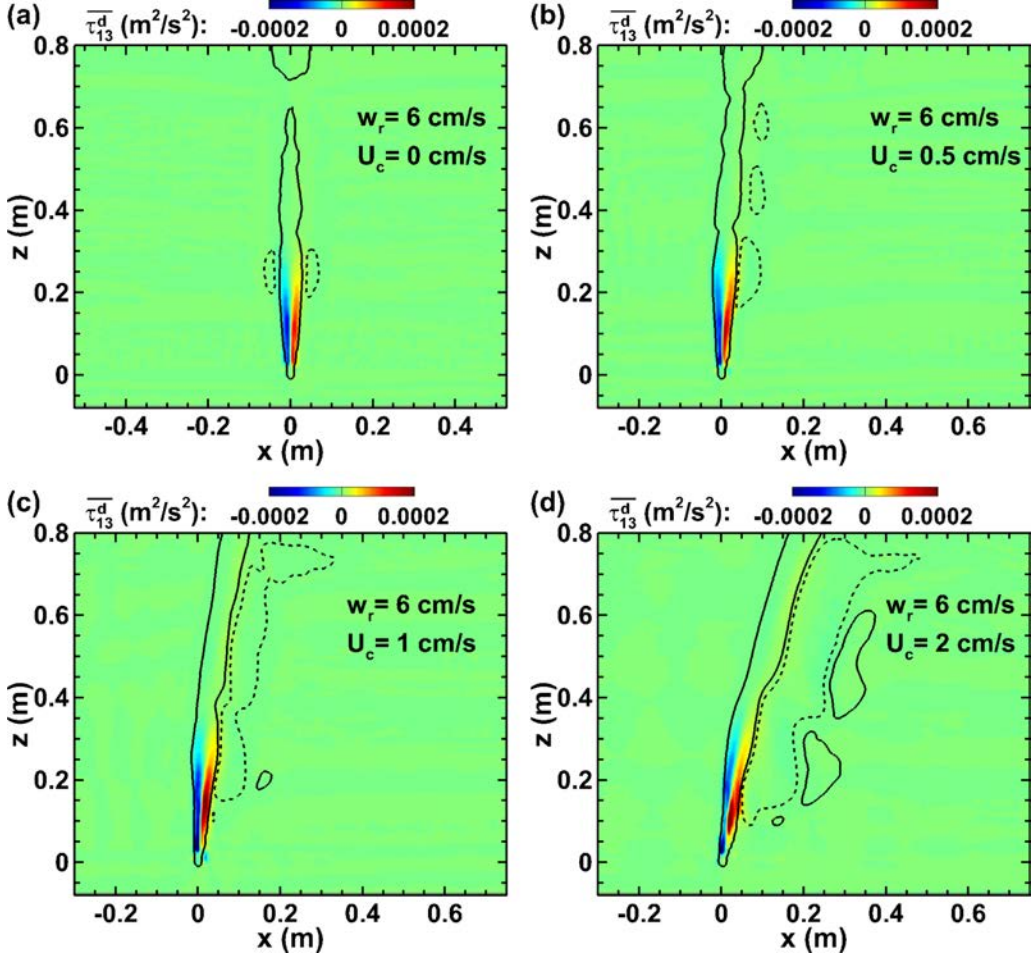


FIG. 14. Time-averaged SGS shear stress $\overline{\tau_{13}^d} = -\overline{v_{sgs}(\partial\tilde{w}/\partial x + \partial\tilde{u}/\partial z)}$ (i.e., the color contours) on the (x, z) -plane across the source for the cases with $w_r = 6$ cm/s: (a) Wr6-Uc0; (b) Wr6-Uc05; (c) Wr6-Uc1; (d) Wr6-Uc2. The solid lines are the isolines of $\tilde{w} = 1$ cm/s, and the dashed lines are the isolines of $\tilde{w} = -1$ cm/s, which are used to indicate the locations of the rising and falling plumes, respectively.

height, more turbulent flow motions are developed due to the unsteady peeling flow and the strong shear between the rising and falling plumes. These turbulent flow motions are directly resolved by the LES model, as indicated by the high value of $\overline{u'w'}$ and low value of $\overline{\tau_{13}^d}$ at about $0.2 \lesssim z \lesssim 0.4$ m (Figs. 14 and 15). Associated with the shift of the falling plume structure from being annular around the rising plume to falling on the downstream side of the plume as U_c increases (Figs. 12 and 13), the turbulent momentum flux $\overline{u'w'}$ also biases towards the downstream side [Figs. 15(b)–15(d)].

Figure 16 shows the time-averaged 3D plumes for the four different bubble rise velocities under the same crossflow condition of $U_c = 2$ cm/s. The corresponding 2D contours of the averaged vertical velocity \tilde{w} on the (x, z) -plane at $y = 0$ m are shown in Fig. 17. As the bubble rise velocity increases, the plume varies from having a strong distinct peeling event in case Wr3-Uc2 to form the isolated falling plume below the peel height [Figs. 16(a) and 17(a)], to having a continuous peeling process in case W20-Uc2 to form the continuous and smooth falling plume from bottom to top along the downstream side of the rising plume [Figs. 16(d) and 17(d)]. For all the four cases shown in Fig. 16, the 2 cm/s crossflow confines the spanwise width of the intrusion region. Cases

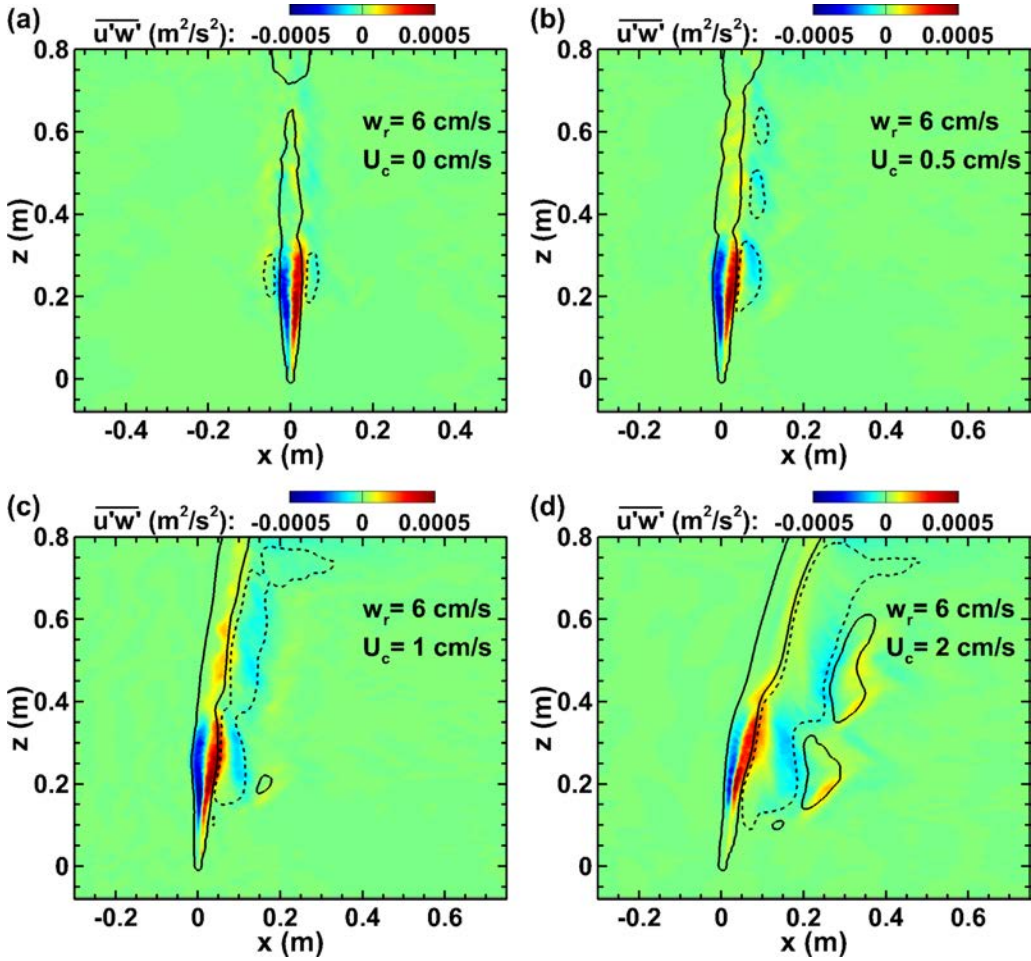


FIG. 15. Time-averaged Reynolds shear stress $\overline{u'w'}$ (i.e., the color contours) on the (x, z) -plane across the source for the cases with $w_r = 6$ cm/s: (a) Wr6-Uc0; (b) Wr6-Uc05; (c) Wr6-Uc1; (d) Wr6-Uc2. The solid lines are the isolines of $\overline{w} = 1$ cm/s, and the dashed lines are the isolines of $\overline{w} = -1$ cm/s, which are used to indicate the locations of the rising and falling plumes, respectively.

Wr3-Uc2 and Wr6-Uc2 exhibit a similar tube-shaped intrusion region [Figs. 16(a) and 16(b)]. In case Wr12-Uc2, the secondary intrusion region can be seen clearly below the primary tube-shaped intrusion region [Fig. 16(c)]. In case Wr20-Uc2, the combined effect of stronger crossflow and continuous peeling process forms a continuous intrusion region (i.e., no separated primary and secondary intrusions) that is narrow in the spanwise direction but tall in the vertical direction [Fig. 16(d)].

The corresponding time-averaged SGS momentum flux $\overline{\tau_{13}^d}$ and resolved turbulent momentum flux $\overline{u'w'}$ for the four cases with $U_c = 2$ cm/s and different w_r are shown in Figs. 18 and 19, respectively. Similar to the results shown in Figs. 14 and 15, $\overline{\tau_{13}^d}$ dominates in the stem region of the rising plume, while $\overline{u'w'}$ becomes dominant at higher elevation near the peel height where the resolved turbulent flow motions are stronger due to the unsteady peeling flow. For all the four different w_r cases, the 2 cm/s crossflow causes $\overline{u'w'}$ to bias towards the downstream side (with respect to the crossflow) of the rising plume where the rising and falling plumes interact. Case

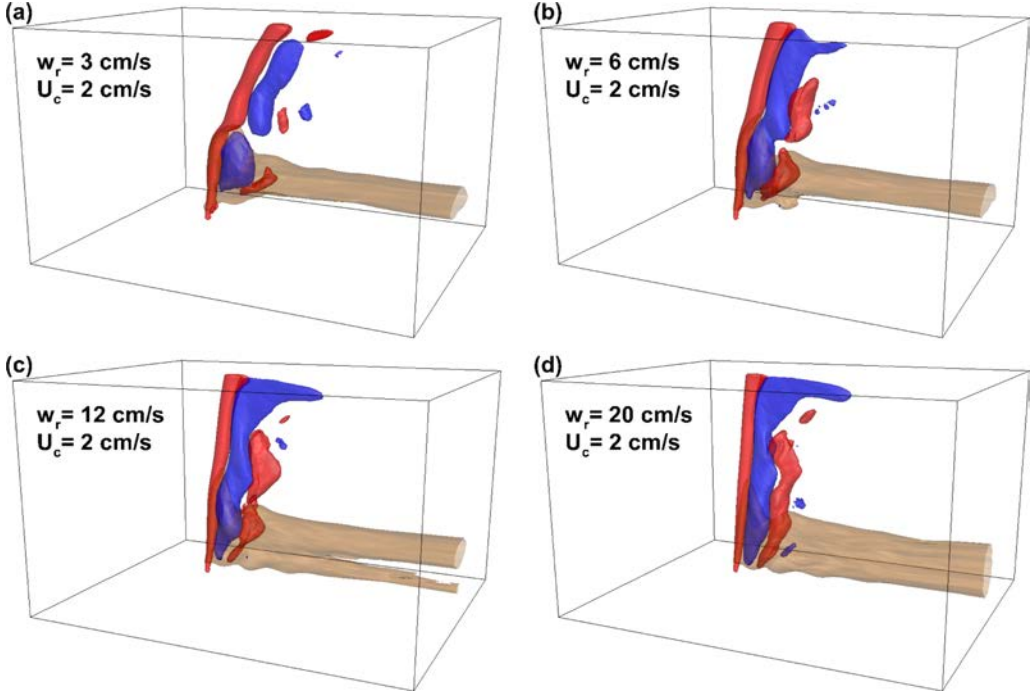


FIG. 16. Time-averaged 3D plumes for $U_c = 2$ cm/s: (a) Wr3-Uc2; (b) Wr6-Uc2; (c) Wr12-Uc2; (d) Wr20-Uc2. The red isosurfaces are for the mean vertical velocity $\bar{w} = 1.5$ cm/s, the blue isosurfaces are for the mean vertical velocity $\bar{w} = -1.5$ cm/s, and the brown isosurfaces are for $\bar{C}_{\text{dye}} = 4$ mg/m³.

Wr20-Uc2 has a narrower and straighter rising plume due to the fast rising bubbles, resulting in a less turbulent rising plume than the other three cases. As a result, both τ_{13}^d and $\overline{u'w'}$ in case Wr20-Uc2 are noticeably weaker than those in the other three cases shown in Figs. 18 and 19. The statistical results shown here are consistent with the weak spatial variation of \bar{w} in case Wr20-Uc2 observed from the instantaneous plume shown in Fig. 8(d).

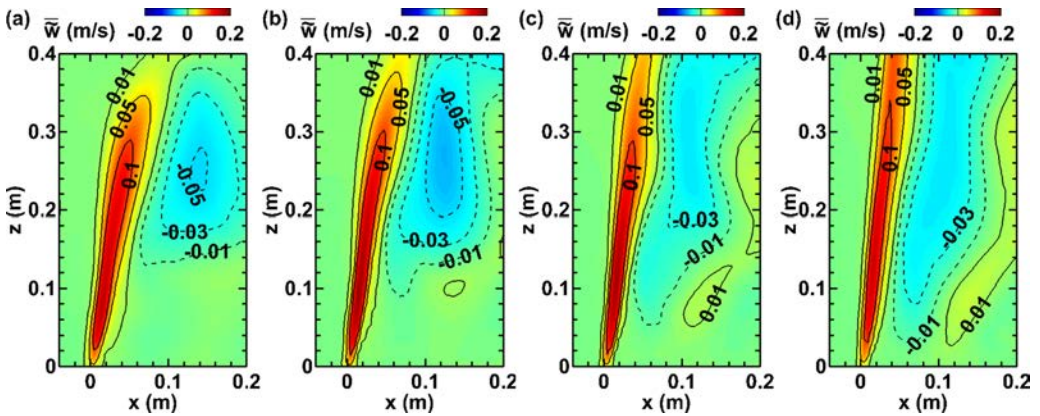


FIG. 17. Time-averaged vertical velocity field on the (x, z) -plane at $y = 0$ m for cases with $U_c = 2$ cm/s: (a) Wr3-Uc2; (b) Wr6-Uc2; (c) Wr12-Uc2; (d) Wr20-Uc2.

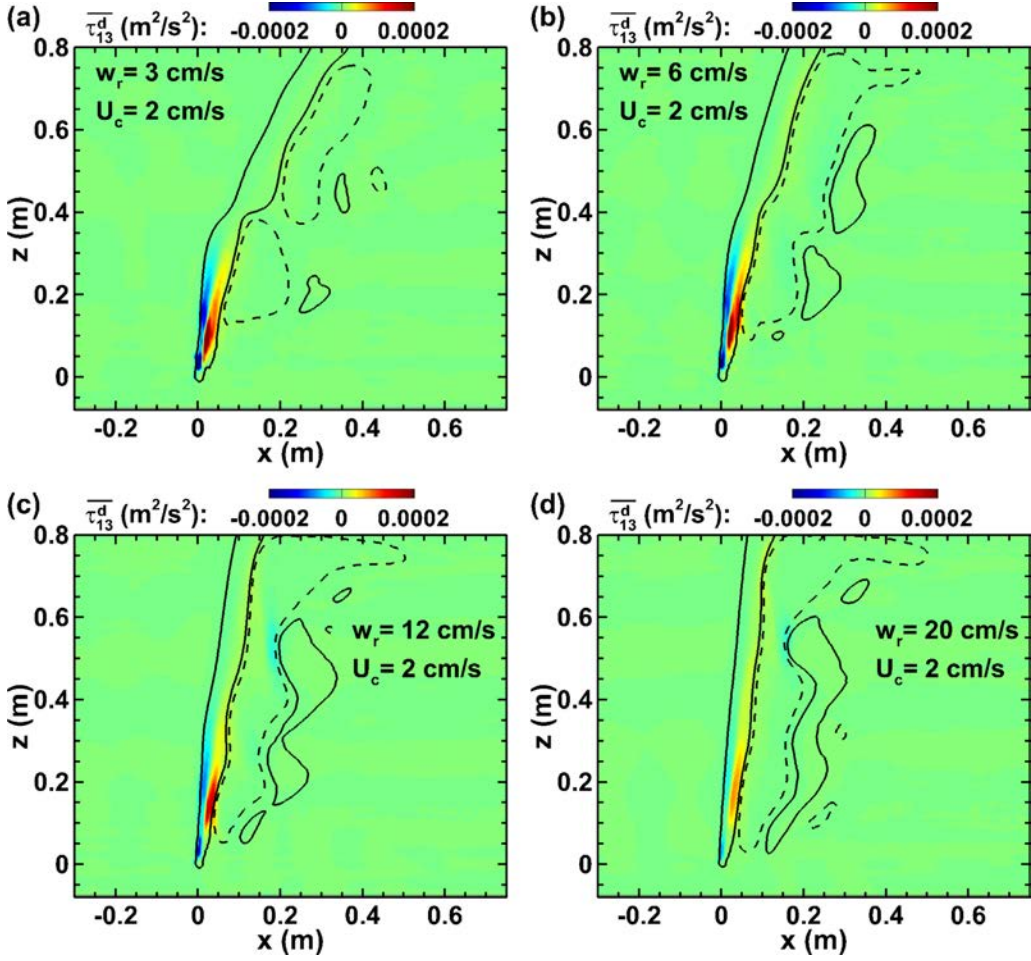


FIG. 18. Time-averaged SGS shear stress $\overline{\tau_{13}^d} = -\overline{v_{sgs}(\partial\tilde{w}/\partial x + \partial\tilde{u}/\partial z)}$ (i.e., the color contours) on the (x, z) -plane across the source for the cases with $U_c = 2$ cm/s: (a) Wr3-Uc2; (b) Wr6-Uc2; (c) Wr12-Uc2; (d) Wr20-Uc2. The solid lines are the isolines of $\tilde{w} = 1$ cm/s, and the dashed lines are the isolines of $\tilde{w} = -1$ cm/s, which are used to indicate the locations of the rising and falling plumes, respectively.

C. Dye flux statistics

Quantifying the characteristics of the plume intrusion layer is crucial for understanding the material transport from the plume to the surrounding environment. One commonly investigated statistics is the averaged elevation of the intrusion layer (i.e., the mean trap height h_t of the detrained water as shown in Fig. 2) [9,11], which can be quantified based on the center-of-mass height of the dye in the intrusion layer [13,14]. For the LES cases with crossflow reported in the present study, h_t is calculated based on the averaged center-of-mass height for the dye concentration at $x \geq 0.5$ m, where the intrusion layer structure has become stable (see Figs. 9 and 10). Figure 20 shows the dimensionless mean plume trap height $H_T = h_t/(B_0/N^3)^{1/4}$ against the dimensionless bubble rise velocity $W_N = w_r/(B_0N)^{1/4}$. Several sets of experimental data for bubble plume in stratified water without crossflow are also plotted in Fig. 20 for comparison. The present LES results fall within the range of the reported experimental data. In general, the data indicate a decreasing trend of H_T when W_N increases. For the LES cases with the two smaller bubble rise velocities ($w_r = 3$ and 6 cm/s, corresponding to $W_N = 0.53$ and 1.06, respectively), increasing the crossflow velocity U_c appears to

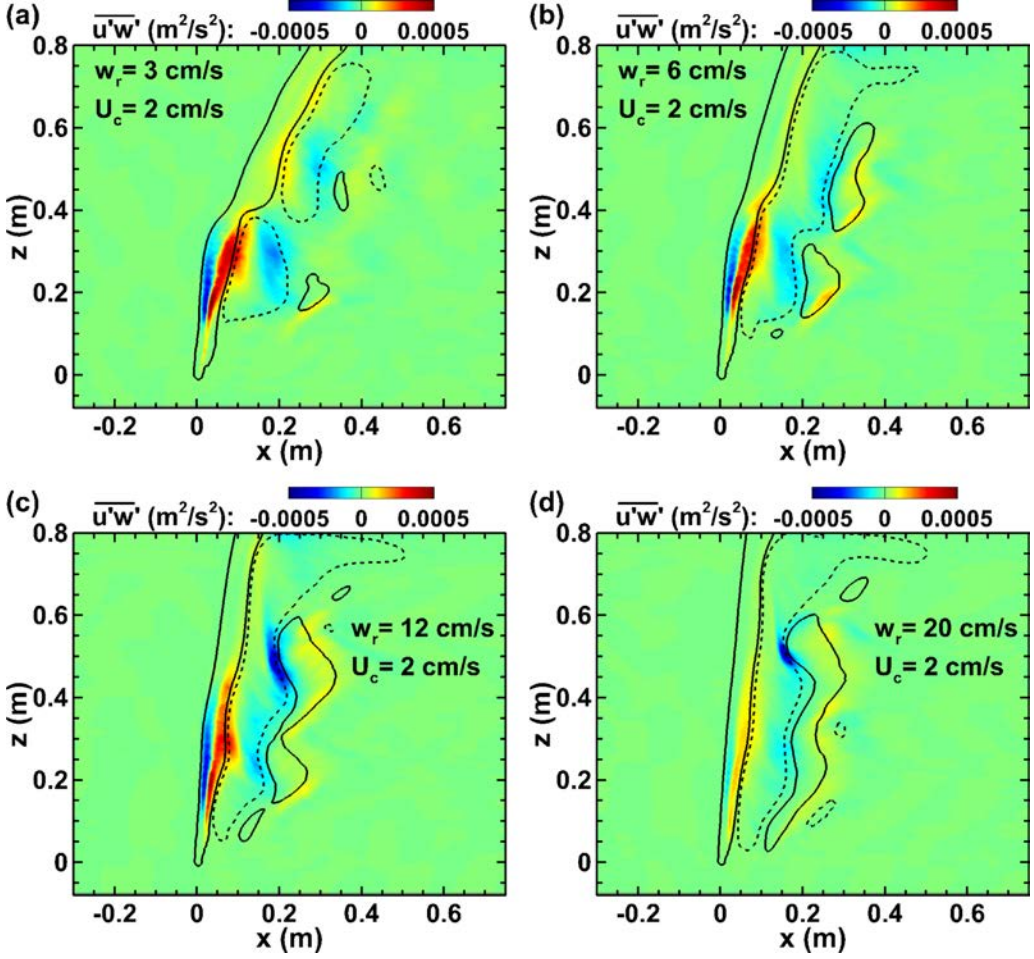


FIG. 19. Time-averaged Reynolds shear stress $\overline{u'w'}$ (i.e., the color contours) on the (x, z) -plane across the source for the cases with $U_c = 2$ cm/s: (a) Wr3-Uc2; (b) Wr6-Uc2; (c) Wr12-Uc2; (d) Wr20-Uc2. The solid lines are the isolines of $\tilde{w} = 1$ cm/s, and the dashed lines are the isolines of $\tilde{w} = -1$ cm/s, which are used to indicate the locations of the rising and falling plumes, respectively.

have a negligible effect on the mean trap height. Differently, for the LES cases with the two larger bubble rise velocities ($w_r = 12$ and 20 cm/s, corresponding to $W_N = 2.12$ and 3.53 , respectively), the LES results show a clear trend that H_T decreases as U_c increases. In particular, case Wr12-Uc2 exhibits a 9% decrease of H_T than case Wr12-Uc05, and case Wr20-Uc2 shows a 24% decrease of H_T than case Wr20-Uc05.

The formation of the intrusion layer and the associated material transport from the plume into the ambient water can be analyzed by quantifying the streamwise flux of dye based on the LES data. Similar to the SGS effect on the vertical momentum exchange shown in Figs. 14 and 18, the SGS flux of dye concentration mainly cause the lateral expansion of the dye concentration field in the stem region of the rising plume (not shown due to space limitation). The transport of dye from the rising plume into the intrusion layer is mainly done through the resolved streamwise flux $\tilde{u}\tilde{C}_{\text{dye}}$. The time-averaged streamwise flux of dye, $\overline{\tilde{u}\tilde{C}_{\text{dye}}}$, can be decomposed as

$$\overline{\tilde{u}\tilde{C}_{\text{dye}}} = \overline{u'C'_{\text{dye}}} + \overline{\tilde{u}\tilde{C}_{\text{dye}}}, \quad (13)$$

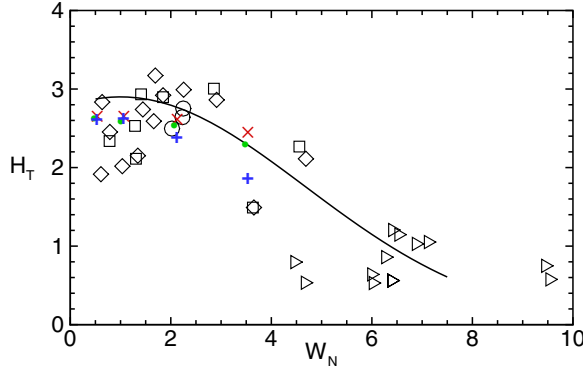


FIG. 20. Nondimensional mean plume trap height $H_T = h_t / (B_0 / N^3)^{1/4}$ as a function of the nondimensional bubble rise velocity $W_N = w_r / (B_0 N)^{1/4}$. Results from the current LES are denoted by solid symbols: \times , cases with crossflow $U_c = 0.5$ cm/s; \bullet , cases with crossflow $U_c = 1.0$ cm/s; $+$, cases with crossflow $U_c = 2.0$ cm/s. The data from various laboratory experiments for plume in stratified water without crossflow are plotted for comparison: \circ , Asaeda and Imberger [4]; \triangleright , Lemckert and Imberger [6]; \diamond , Socolofsky [67]; and \square , Socolofsky and Adams [9]. The empirical parametrization from Socolofsky and Adams [9] is denoted by —.

where $u' = \tilde{u} - \bar{u}$ is the turbulent fluctuation of the streamwise velocity and $C'_{\text{dye}} = \tilde{C}_{\text{dye}} - \bar{C}_{\text{dye}}$ is the turbulent fluctuation of the dye concentration. In Eq. (13), $\overline{u'C'_{\text{dye}}}$ represents the turbulent entrainment due to the streamwise velocity fluctuation and $\overline{\tilde{u}\tilde{C}_{\text{dye}}}$ represents the dye transport by the mean streamwise flow.

Figures 21 and 22 show the contours of $\overline{u'C'_{\text{dye}}}$ and $\overline{\tilde{u}\tilde{C}_{\text{dye}}}$, respectively, on the (x, z) -plane across the plume source for $w_r = 6$ cm/s under different crossflow conditions. Note that the contour range plotted in Fig. 22 is four times the range plotted in Fig. 21. For case Wr6-Uc0 (i.e., no crossflow), strong horizontal turbulent fluxes of dye concentration appear within the stem region of the rising plume (i.e., at $z \lesssim 0.2$ m) [Fig. 21(a)], which cause the radial expansion of the dye concentration field as the plume rises through the water. At $0.2 \lesssim z \lesssim 0.3$ m, the rising plume (i.e., the region enclosed by the isoline of $\bar{w} = 1$ cm/s) interacts with the falling plume (indicated by the isolines of $\bar{w} = -1$ cm/s), resulting in strong turbulent entrainment flux of dye across the interface of the two counterflowing plume regions [Fig. 21(a)]. At $0.3 \lesssim z \lesssim 0.4$ m, strong horizontal turbulent flux of dye also occurs due to the turbulence in the plume peeling process [Fig. 21(a)]. After the dye is detrained from the rising plume, it is carried by the falling plume to the neutral buoyancy level and further transported into the horizontal intrusion layer by the relatively weak radial direction mean flow, as shown by the mean horizontal flux in Fig. 22(a).

With the presence of crossflow, the peeling process forms the falling plume on the downstream side of the rising plume, causing the turbulent entrainment process to also bias towards the downstream side [Figs. 21(b)–21(d)]. For case Wr6-Uc05 with the weak crossflow of $U_c = 0.5$ cm/s, the turbulent flux $\overline{u'C'_{\text{dye}}}$ plays a dominant role in transporting the dye from the rising plume into the falling plume through the primary peeling flow as well as across the rising/falling plume interface via turbulent entrainment [Fig. 21(b)]. After the dye is carried to the neutral buoyancy level by the falling plume, the streamwise flux $\overline{\tilde{u}\tilde{C}_{\text{dye}}}$ due to the mean flow becomes dominant and continues to transport the dye into the horizontal intrusion layer at around $z = 0.2$ m [Fig. 22(b)]. As the crossflow velocity further increases to $U_c = 1$ cm/s (i.e., case Wr6-Uc1), while the turbulent flux $\overline{u'C'_{\text{dye}}}$ is still significant in the peeling flow region [Fig. 21(c)], the mean flow flux $\overline{\tilde{u}\tilde{C}_{\text{dye}}}$ also makes a considerable contribution for transporting the dye from the rising plume into the falling plume near the peeling region [Fig. 22(c)]. Noticeable mean flux is also observed at a lower elevation to transport the dye into the secondary intrusion layer at around $z = 0.08$ m. As the crossflow

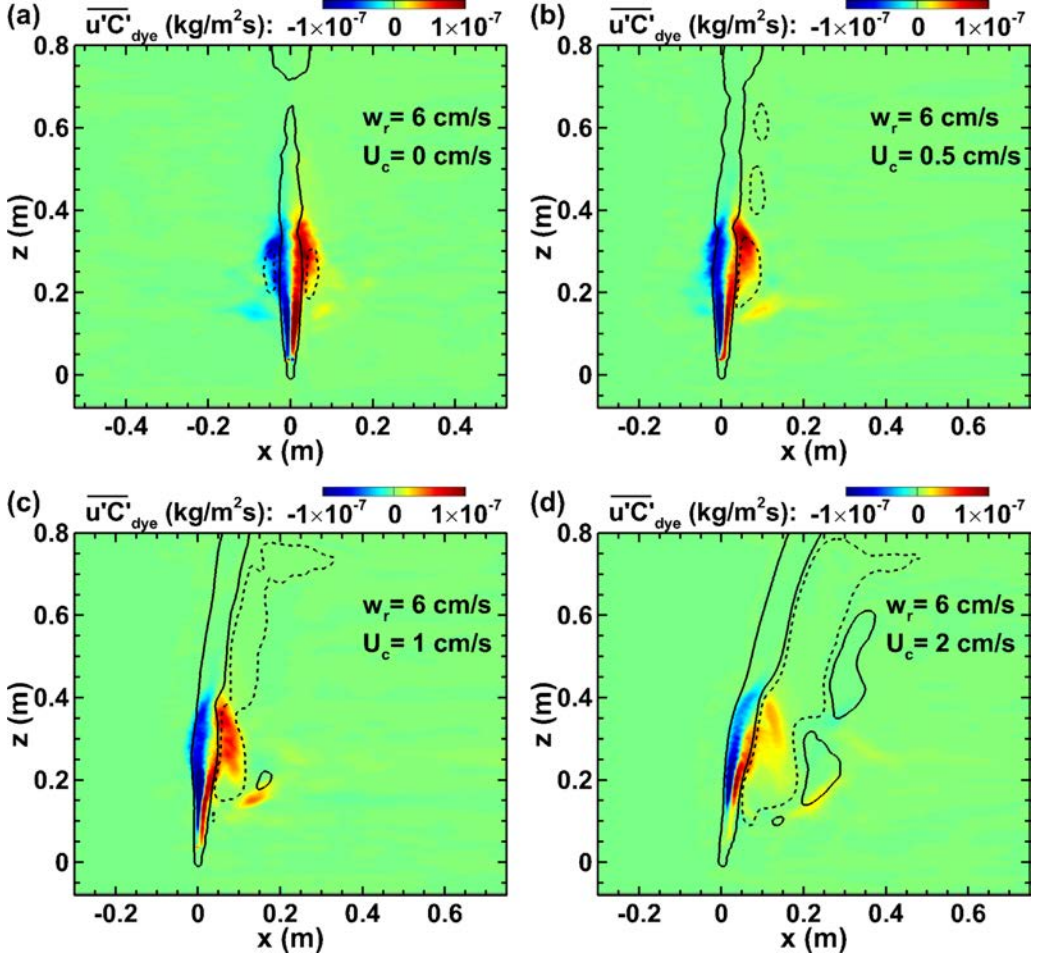


FIG. 21. Time-averaged streamwise dye entrainment flux $\overline{u'C'_{\text{dye}}}$ (i.e., the color contours) on the (x, z) -plane across the source for the cases with $w_r = 6$ cm/s: (a) Wr6-Uc0; (b) Wr6-Uc05; (c) Wr6-Uc1; (d) Wr6-Uc2. The solid lines are the isolines of $\widetilde{w} = 1$ cm/s, and the dashed lines are the isolines of $\widetilde{w} = -1$ cm/s, which are used to indicate the locations of the rising and falling plumes, respectively.

further increases to $U_c = 2$ cm/s in case Wr6-Uc2, the inclined rising plume generates a more steady peeling flow at around $z = 0.4$ m, resulting in weaker turbulent flux $\overline{u'C'_{\text{dye}}}$ [Fig. 21(d)] and more significant mean flux [Fig. 22(d)] from the rising plume into the falling plume near the peeling region. Further downstream from the plume, the dye is transported into both the primary and secondary intrusion layers by the mean streamwise velocity, with more significant mean flux into the primary intrusion layer [Fig. 22(d)].

Figures 23 and 24 show the contours of $\overline{u'C'_{\text{dye}}}$ and $\overline{\widetilde{u}\widetilde{C}'_{\text{dye}}}$, respectively, on the (x, z) -plane across the plume source for the four different bubble rise velocities under the same crossflow condition of $U_c = 2$ cm/s. Note that similar to Figs. 21 and 22, the contour range plotted in Fig. 23 is four times the range plotted in Fig. 24. The analysis result shows that the turbulent and mean dye fluxes for cases Wr3-Uc2 and Wr6-Uc2 are similar in general, exhibiting a strong peeling process near $z = 0.4$ m with considerable turbulent and mean dye fluxes from the rising plume into the falling plume [Figs. 23(a), 23(b), 24(a), and 24(b)]. For case Wr12-Uc2 with a larger bubble rise velocity of $w_r = 12$ cm/s [Figs. 23(c) and 24(c)], the rising plume is narrower and straighter, and the main

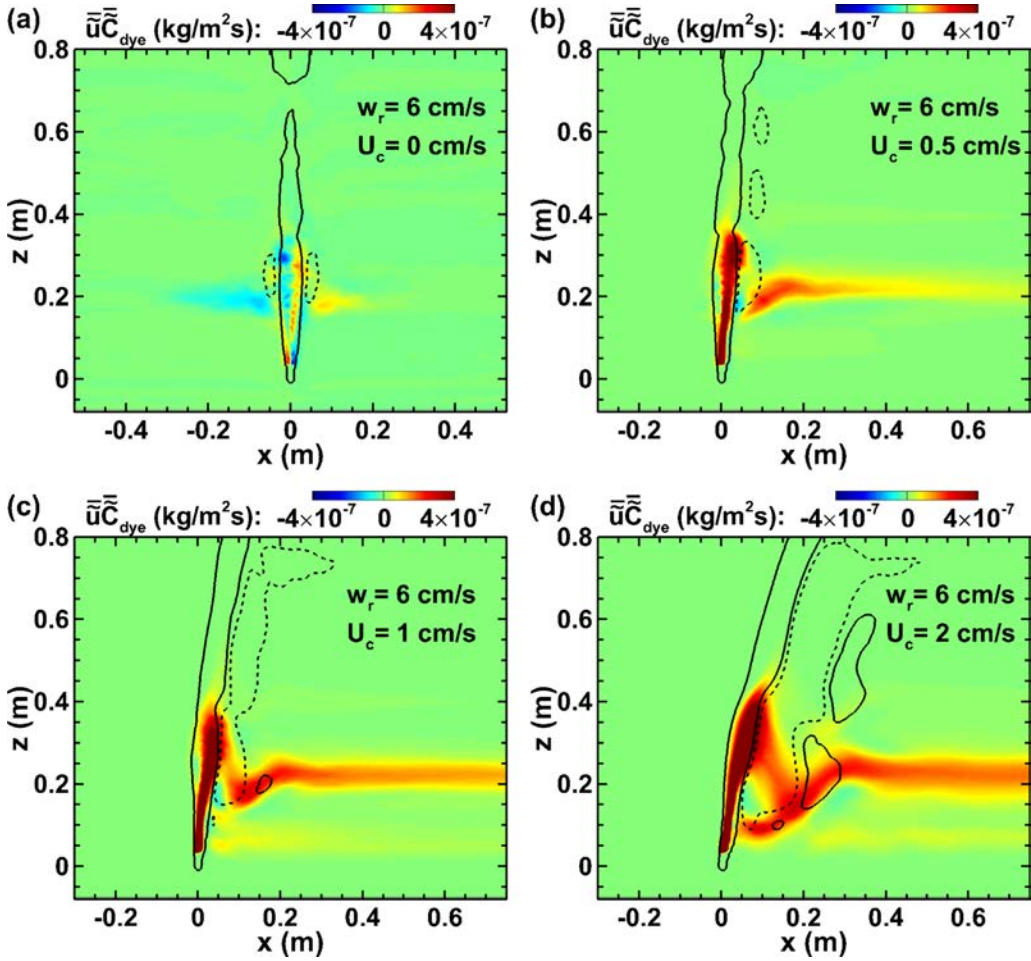


FIG. 22. Time-averaged streamwise dye flux by mean flow $\overline{\tilde{u}\tilde{C}}_{\text{dye}}$ (i.e., the color contours) on the (x, z) -plane across the source for the cases with $w_r = 6$ cm/s: (a) Wr6-Uc0; (b) Wr6-Uc05; (c) Wr6-Uc1; (d) Wr6-Uc2. The solid lines are the isolines of $\tilde{w} = 1$ cm/s, and the dashed lines are the isolines of $\tilde{w} = -1$ cm/s, which are used to indicate the locations of the rising and falling plumes, respectively.

peeling process occurs at a lower elevation of around $z = 0.3$ m, with considerable contributions due to both the turbulent and mean dye fluxes from the rising plume into the falling plume. The mean dye flux into the secondary intrusion layer in case Wr12-Uc2 is also larger than those in cases Wr3-Uc2 and Wr6-Uc2. Differently, case Wr20-Uc2 does not exhibit a strong and distinct primary peeling process, as shown by the vertically distributed weak turbulent dye flux from the rising plume into the falling plume within $0.1 \lesssim z \lesssim 0.4$ m [Fig. 23(d)]. On the other hand, the mean dye flux is significant along the downstream side of the rising plume in case Wr20-Uc2 [Fig. 24(d)]. The combined effect of the turbulent and mean fluxes of dye results in the vertically extended intrusion region in case Wr20-Uc2 shown in Figs. 10(d) and 16(d).

Further downstream away from the rising and falling plumes, the dye is transported mainly by the mean streamwise flow. Based on the time-averaged flow field, the mean streamwise flux of the dye concentration can be quantified to help understand the spatial distribution of mean intrusion from the plume into the water in the far field. In particular, the total mean streamwise flux of dye

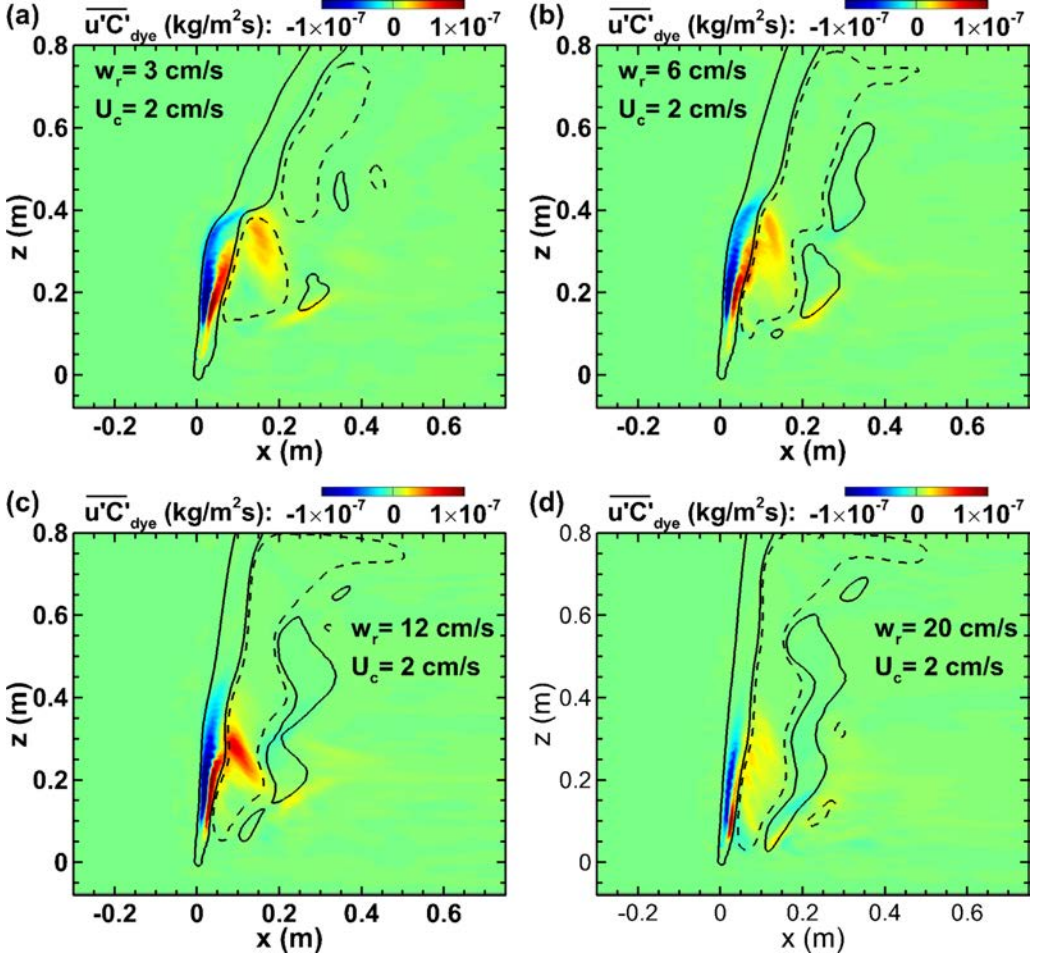


FIG. 23. Time-averaged streamwise dye entrainment flux $\overline{u'C'_{\text{dye}}}$ (i.e., the color contours) on the (x, z) -plane across the source for the cases with $U_c = 2$ cm/s: (a) Wr3-Uc2; (b) Wr6-Uc2; (c) Wr12-Uc2; (d) Wr20-Uc2. The solid lines are the isolines of $\tilde{w} = 1$ cm/s, and the dashed lines are the isolines of $\tilde{w} = -1$ cm/s, which are used to indicate the locations of the rising and falling plumes, respectively.

across the (y, z) -plane at the streamwise location x_0 can be calculated as

$$\Phi_x = \int_{z_{\text{bot}}}^{z_{\text{top}}} \int_{-L_y/2}^{L_y/2} \tilde{u}(x_0, y, z) \tilde{C}_{\text{dye}}(x_0, y, z) dy dz, \quad (14)$$

where the domain dimension parameters z_{bot} , z_{top} and L_y are specified in Sec. III. The normalized vertical distribution of the mean streamwise dye flux is defined as

$$\phi_x(z) = \frac{1}{\Phi_x} \int_{-L_y/2}^{L_y/2} \tilde{u}(x_0, y, z) \tilde{C}_{\text{dye}}(x_0, y, z) dy, \quad (15)$$

and the normalized spanwise distribution of the mean streamwise dye flux is

$$\psi_x(y) = \frac{1}{\Phi_x} \int_{z_{\text{bot}}}^{z_{\text{top}}} \tilde{u}(x_0, y, z) \tilde{C}_{\text{dye}}(x_0, y, z) dz. \quad (16)$$

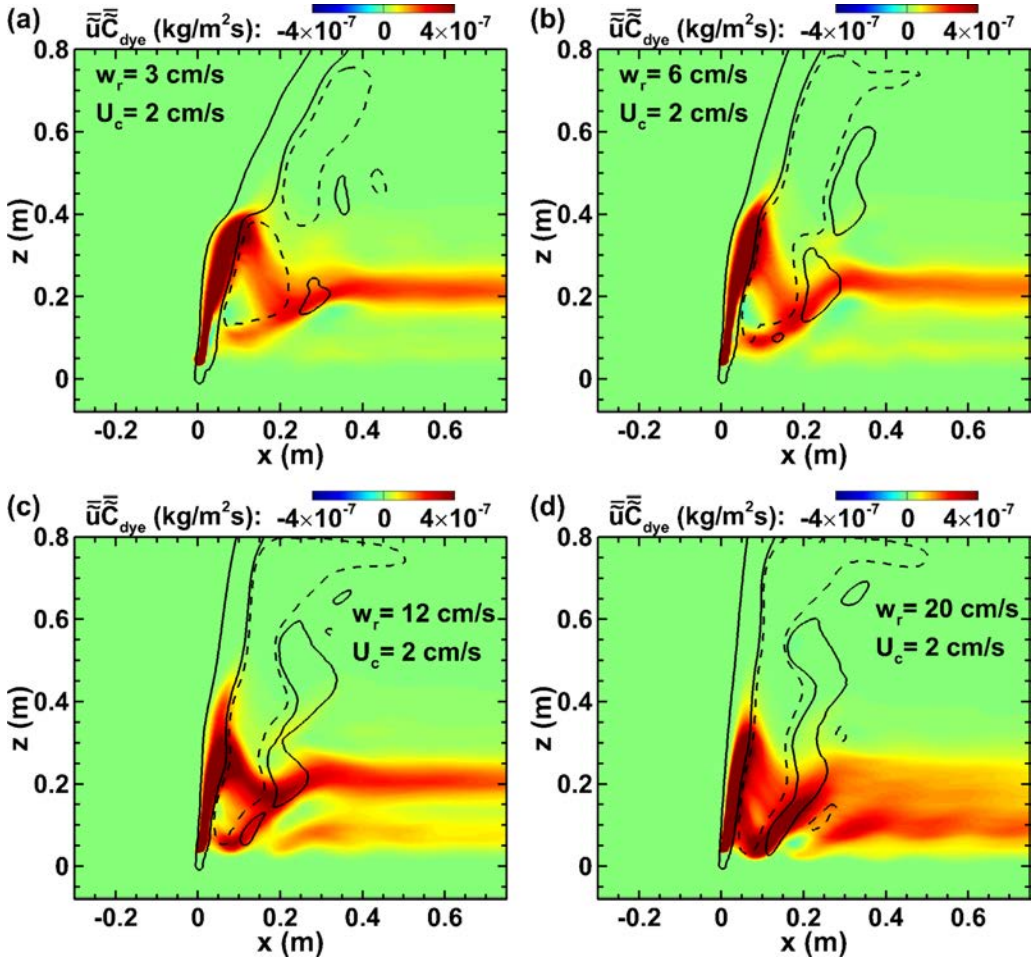


FIG. 24. Time-averaged streamwise dye flux by mean flow $\bar{u}\bar{C}_{dye}$ (i.e., the color contours) on the (x, z) -plane across the source for the cases with $U_c = 2$ cm/s: (a) Wr3-Uc2; (b) Wr6-Uc2; (c) Wr12-Uc2; (d) Wr20-Uc2. The solid lines are the isolines of $\bar{w} = 1$ cm/s, and the dashed lines are the isolines of $\bar{w} = -1$ cm/s, which are used to indicate the locations of the rising and falling plumes, respectively.

Figures 25 and 26 show the profiles of $\phi_x(z)$ and $\psi_x(y)$, respectively, for the LES cases with the four different bubble rise velocities and three different crossflow velocities. The results at two representative streamwise locations, $x_0 = 0.5$ m and 0.6 m, are shown in both figures. As suggested by the contours of $\bar{u}\bar{C}_{dye}$ shown in Figs. 22 and 24, the influence from the rising and falling plumes on the mean streamwise flux of dye becomes insignificant at $x \geq 0.5$ m. The profiles of mean streamwise dye flux at $x_0 = 0.5$ m and 0.6 m shown in Figs. 25 and 26 show good agreement, confirming that setting $x_0 \geq 0.5$ m is sufficient for characterizing $\phi_x(z)$ and $\psi_x(y)$ without significant influence from the buoyant plume dynamics.

Several general trends observed from the instantaneous and time-averaged plume fields can be seen clearly here from these mean dye flux profiles shown in Figs. 22 and 24. On the one hand, for a fixed U_c , increasing w_r causes the primary intrusion region to spread more in the vertical direction and less in the spanwise direction. The enhanced vertical spreading of $\phi_x(z)$ for plumes with large w_r is mainly caused by their unstable peeling processes that leak the dye into the crossflow over a range of vertical elevations. The suppressed spanwise spreading of $\psi_x(y)$ for plumes with larger

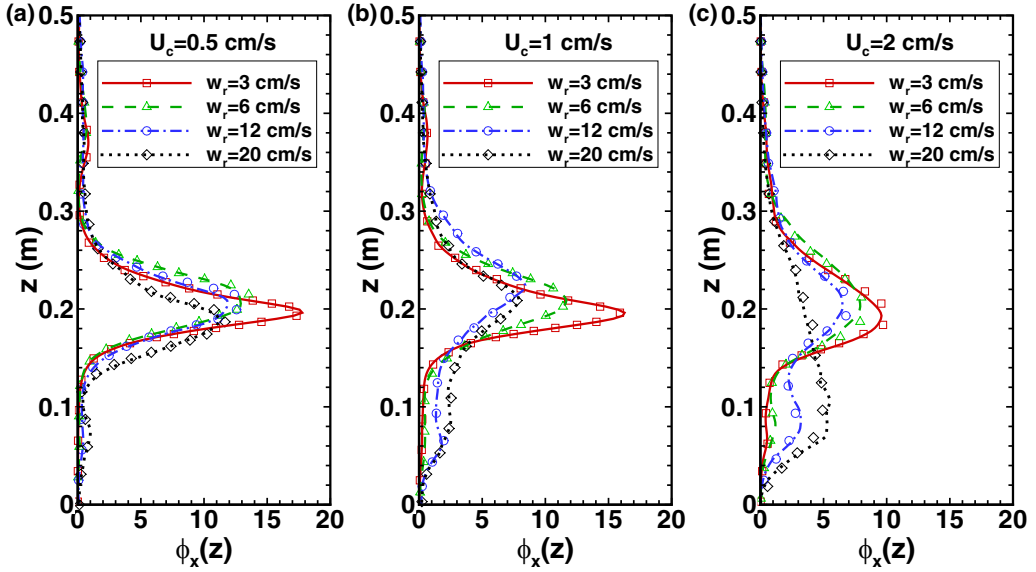


FIG. 25. Normalized vertical distributions of mean streamwise dye flux $\phi_x(z)$ at $x_0 = 0.5$ m (lines) and $x_0 = 0.6$ m (symbols): (a) cases with $U_c = 0.5$ m/s; (b) cases with $U_c = 1$ m/s; (c) cases with $U_c = 2$ m/s.

w_r is mainly caused by the decrease of peeling flow intensity as w_r increases [14]. The interaction between the horizontal flow motions of the peeling process and the crossflow can be qualitatively explained by making an analogy with the classical ideal flow for a source in a uniform stream [68], for which the spanwise width of the wake region behind the source is proportional to the ratio between the strength of the source and the uniform stream velocity. For the plume conditions

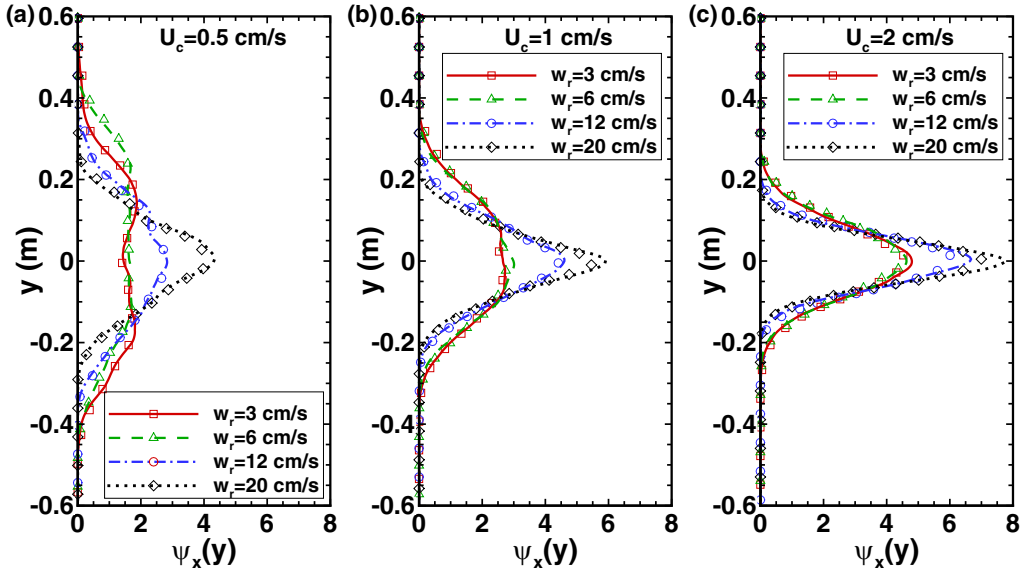


FIG. 26. Normalized spanwise distributions of mean streamwise dye flux $\psi_x(y)$ at $x_0 = 0.5$ m (lines) and $x_0 = 0.6$ m (symbols): (a) cases with $U_c = 0.5$ m/s; (b) cases with $U_c = 1$ m/s; (c) cases with $U_c = 2$ m/s.

considered in the present study, a plume with larger w_r has a smaller radial velocity associated with the weaker peeling process [14], resulting in less spanwise spreading of the intrusion layer under the same crossflow condition.

On the other hand, for a fixed w_r , increasing the crossflow velocity U_c results in the intrusion region being spread more vertically and less spanwise. Similar to the aforementioned analogy with a source in a uniform stream, the suppressed spanwise spreading of the intrusion region as U_c increases is caused by the decreased ratio of the peeling flow horizontal velocity to crossflow velocity. The enhanced vertical spreading of the intrusion region is caused by the enhanced mean peeling flow from the rising plume to the falling plume (Fig. 22). The enhanced falling plume when U_c increases (Figs. 11 and 12) also helps to bring more dye from the peel height down to some lower elevation. Large w_r (e.g., 12 and 20 cm/s) also results in noticeable secondary intrusion below $z = 0.1$ m, which becomes more significant when combined with the effect of fast crossflows (e.g., $U_c = 1$ and 2 cm/s). For case Wr20-Uc2, the profile ϕ_x [the dotted line in Fig. 25(c)] exhibits a wide vertical distribution of the mean streamwise dye flux within $0 < z < 0.4$ m, with the peak near $z = 0.1$ m that is much lower than the primary peak elevation of ϕ_x in other cases (i.e., near $z = 0.2$ m). This shift of main intrusion flux towards the lower elevation in case Wr20-Uc2 is caused by the combination of two effects. First, the fast rising bubbles with $w_r = 2$ cm/s forms a narrow rising plume that is weak for lifting the entrained water to higher elevation, resulting in irregular and unstable peeling process at lower elevation instead of forming a distinct peeling event at higher elevation (Figs. 7 and 8). Second, the combined effect of the narrow rising plume and the strong crossflow of $U_c = 2$ cm/s in case Wr20-Uc2 results in a significant mean flux of dye from the rising plume into the falling plume [Fig. 24(d)]. The strong falling plume can reach as low as $z = 0.04$ m [Fig. 17(d)], during which the water inside the falling plume mixes with the higher density ambient water at lower elevation, resulting in a lower elevation for the main intrusion layer where the mixed water reaches the equilibrium density level.

V. CONCLUSIONS

In this study, a LES model is applied to simulate bubble-driven turbulent plumes in the stably stratified water with weak crossflows. A series of LES runs have been performed to cover a range of plume and crossflow conditions, including four different bubble rise velocities ($w_r = 3, 6, 12$ and 20 cm/s) and three different crossflow velocities (i.e., $U_c = 0.5, 1$ and 2 cm/s). The effects of crossflow on the plume dynamics and material transport are studied by both direct observations of the instantaneous plume fields and statistical analysis of the time-averaged plume characteristics.

A bubble-driven plume released in a stably stratified quiescent water is known to generate a statistically axisymmetric double-plume structure, consisting of an inner rising plume of bubble/water mixture and an annular outer plume of detrained water (due to the density stratification) falling along the outside of the inner plume. The key mechanism for the weak crossflow to affect the plume dynamics is to tilt the plume towards the downstream direction of the crossflow and break the axisymmetry of the dynamics. The LES results show that the crossflow causes the falling plume to form on the downstream side of the rising plume, resulting in reduced overall contact area and turbulent entrainments between the two plumes. With the reduced turbulent mixing of momentum, both the rising and falling plumes exhibit increased vertical velocity as the crossflow speed increases.

The effect of crossflow on the material transport from the plume into the surrounding environment (through the horizontal intrusion layer of detrained fluid) is studied by characterizing the dye tracer concentration field. The LES results show that the crossflow suppresses the lateral spreading and enhances the vertical spreading of the intrusion layer. The lateral spreading of the intrusion flow in crossflow exhibits analogy to that of a source in a uniform stream. In particular, the crossflow suppresses the upstream and transverse expansions of the intrusion layer and forces it to expand primarily towards the downstream direction of the crossflow. Increasing the crossflow speed causes the lateral width of the intrusion layer to reduce. The vertical spreading of the intrusion layer in

crossflow is more complicated due to the combination of several effects, including the stability of the plume peeling process, the speed of the falling plume, and the enhanced mean mass flux from the rising plume to the falling plume due to the crossflow. In general, the crossflow tends to enhance the vertical spreading of the intrusion layer and generate more noticeable horizontal dye flux at lower elevation, especially for the plumes of large bubbles that have irregular and unstable peeling process.

It should be noted that the present study considers the laboratory-scale condition with relatively simple water stratification and crossflow conditions. Therefore, caution should be taken when applying the conclusion from the present study to the case of a field-scale plume. Further investigations are desired for understanding the crossflow effect on a large-scale bubble-driven plume in the deep-water environment, with additional effects to be taken into consideration (e.g., the depth-dependent variation of the crossflow velocity, the nonlinear stratification of water density, the effects of gas bubble expansion and dissolution when rising through the large water depth, etc.). Nevertheless, the simulation and statistical analysis results reported in this study still provide some useful insights for understanding some of the key effects of the crossflow on the plume dynamics and material transport.

ACKNOWLEDGMENTS

D.Y. acknowledges the financial support from his start-up funds as well as the computational resources from the Research Computing Center (RCC) and the Research Computing Data Core (RCDC) at the University of Houston.

APPENDIX A: DERIVATION OF PLUME FLOW LES MODEL GOVERNING EQUATION

In this Appendix, the derivation of the LES model equation (3) is briefly discussed. Following several recent LES studies, the momentum carried by the bubble phase is assumed to be negligible [14,15,25,34]. The Eulerian momentum transport equation governing the water phase of the plume can be written as [15,25]

$$\frac{\partial[(1 - \alpha_b)\rho\mathbf{u}]}{\partial t} + \nabla \cdot [(1 - \alpha_b)\rho\mathbf{u}\mathbf{u}] = -\nabla p + \nabla \cdot [2(1 - \alpha_b)\rho\nu\mathbf{S}] - (1 - \alpha_b)\rho g\mathbf{e}_z - \alpha_b\rho_b g\mathbf{e}_z, \quad (\text{A1})$$

where α_b is the local void fraction of the gas bubbles, ν is the kinematic viscosity of water, and $\mathbf{S} = [\nabla\mathbf{u} + (\nabla\mathbf{u})^T]/2$ is the strain rate tensor. The definitions of other symbols are given in Sec. II. Equation (A1) governs the momentum transport of the water phase.

The instantaneous local water density $\rho(\mathbf{x}, t)$ varies in time and space due to the interaction between the bubble-driven plume and the ambient stratified water. It can be decomposed as

$$\rho(\mathbf{x}, t) = \langle \rho(\mathbf{x}, t) \rangle_h + \rho'(\mathbf{x}, t), \quad (\text{A2})$$

where $\langle \rho(\mathbf{x}, t) \rangle_h$ is the horizontal average of $\rho(\mathbf{x}, t)$, and $\rho'(\mathbf{x}, t)$ is the instantaneous local density perturbation caused by the plume flow motion. The horizontal average density $\langle \rho(\mathbf{x}, t) \rangle_h$ can be further decomposed as

$$\langle \rho(\mathbf{x}, t) \rangle_h = \rho_0 + \rho''(z, t), \quad (\text{A3})$$

where ρ_0 is a constant reference density of water and $\rho''(z, t)$ is the background density variation in the vertical direction and in time. For the flow condition considered in the present study, the density components satisfy $\rho'(\mathbf{x}, t) + \rho''(z, t) \ll \rho_0$, which allows us to apply the Boussinesq approximation [69–72] to simplify Eq. (A1) as

$$\frac{\partial[(1 - \alpha_b)\mathbf{u}]}{\partial t} + \nabla \cdot [(1 - \alpha_b)\mathbf{u}\mathbf{u}] = -\frac{1}{\rho_0}\nabla p + \nabla \cdot [2(1 - \alpha_b)\nu\mathbf{S}] - \frac{\rho}{\rho_0}(1 - \alpha_b)g\mathbf{e}_z - \frac{\rho_b}{\rho_0}\alpha_b g\mathbf{e}_z. \quad (\text{A4})$$

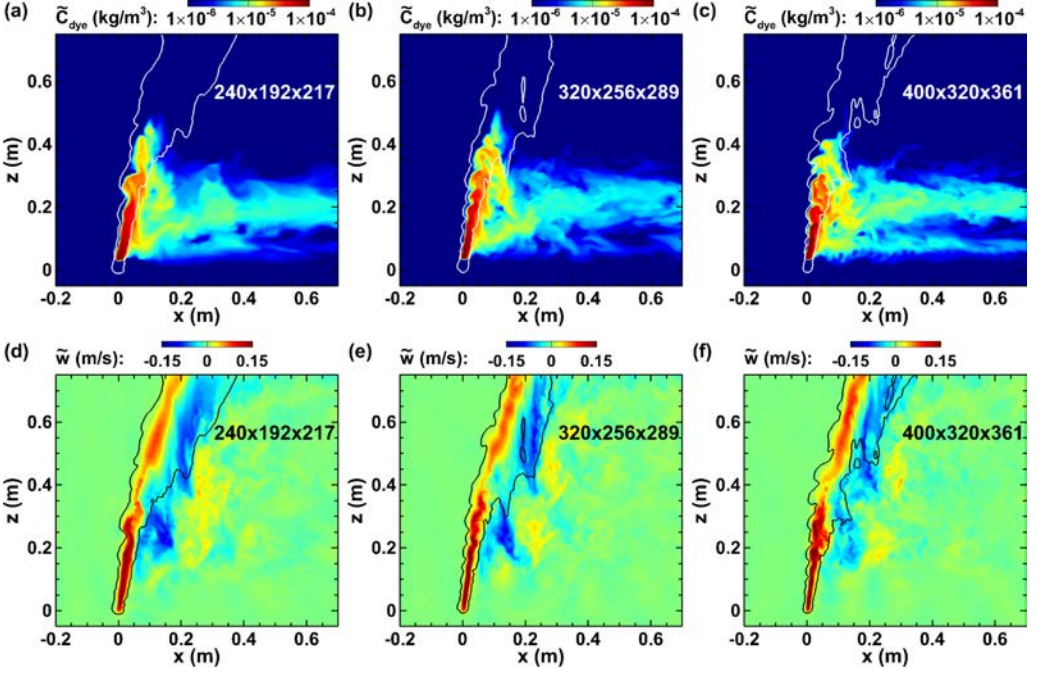


FIG. 27. Instantaneous plumes on the (x, z) -plane across the source location at $t = 100$ s for case Wr6-Uc2 ($w_r = 6$ cm/s, $U_c = 2$ cm/s) obtained from LES with different grid numbers $N_x \times N_y \times N_z =$: (a), (d) $240 \times 192 \times 217$; (b), (e) $320 \times 256 \times 289$; (c), (f) $400 \times 320 \times 361$. The top row shows the color contours of the time-averaged dye concentration \tilde{C}_{dye} , and the bottom row shows the color contours of the resolved instantaneous vertical velocity \tilde{w} . In each panel, the solid lines are the isolines of $\tilde{C}_b = 0.001$ kg/m³, which are used to indicate the shape and location of the bubble column.

By rewriting the pressure gradient term based on the dynamic pressure $p^* = p + \rho_0 g z$, Eq. (A4) can be rewritten as

$$\begin{aligned} \frac{\partial[(1 - \alpha_b)\mathbf{u}]}{\partial t} + \nabla \cdot [(1 - \alpha_b)\mathbf{u}\mathbf{u}] = & -\frac{1}{\rho_0} \nabla p^* + \nabla \cdot [2(1 - \alpha_b)\nu\mathbf{S}] \\ & + \left(1 - \frac{\rho}{\rho_0}\right)(1 - \alpha_b)g\mathbf{e}_z + \left(1 - \frac{\rho_b}{\rho_0}\right)\alpha_b g\mathbf{e}_z. \end{aligned} \quad (\text{A5})$$

By assuming $\alpha_b \ll 1$ under low bubble void fraction condition, Eq. (A5) can be further approximated as

$$\frac{\partial\mathbf{u}}{\partial t} + \nabla \cdot (\mathbf{u}\mathbf{u}) = -\frac{1}{\rho_0} \nabla p^* + \nabla \cdot (2\nu\mathbf{S}) + \left(1 - \frac{\rho}{\rho_0}\right)g\mathbf{e}_z + \left(1 - \frac{\rho_b}{\rho_0}\right)\alpha_b g\mathbf{e}_z. \quad (\text{A6})$$

Substituting $\alpha_b = C_b/\rho_b$ into Eq. (A6) and applying the spatial filtering yields

$$\frac{\partial\tilde{\mathbf{u}}}{\partial t} + \tilde{\mathbf{u}} \cdot \nabla\tilde{\mathbf{u}} = -\frac{1}{\rho_0} \nabla p^* - \nabla \cdot \boldsymbol{\tau} + \nabla \cdot (2\nu\tilde{\mathbf{S}}) + \left(1 - \frac{\tilde{\rho}}{\rho_0}\right)g\mathbf{e}_z + \left(1 - \frac{\rho_b}{\rho_0}\right)\frac{\tilde{C}_b}{\rho_b}g\mathbf{e}_z, \quad (\text{A7})$$

where $\boldsymbol{\tau} = \tilde{\mathbf{u}}\tilde{\mathbf{u}} - \tilde{\mathbf{u}}\tilde{\mathbf{u}}$ is the SGS stress tensor. For the turbulent plume flow considered in the present study, the viscous stress due to the resolved strain rate, $\tau_v = 2\nu\tilde{\mathbf{S}}$, is much smaller than the SGS stress $\boldsymbol{\tau}$. By neglecting τ_v and absorbing the trace of $\boldsymbol{\tau}$ into the pressure gradient term, Eq. (A7) can be rewritten as Eq. (3), which is used in the present LES model to simulated the bubble-driven plume flow.

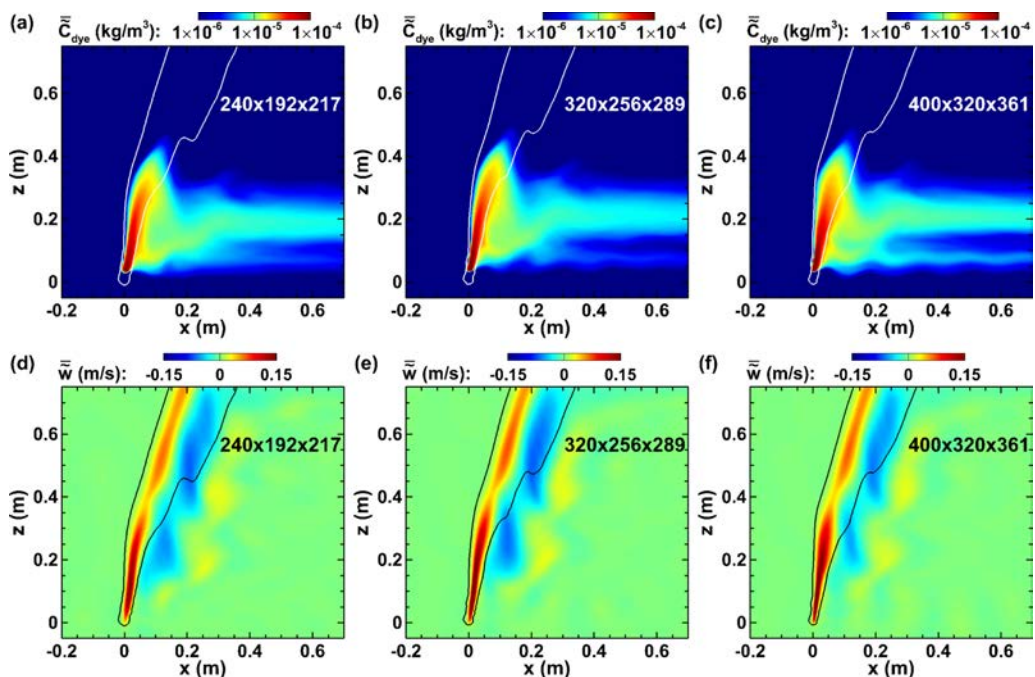


FIG. 28. Time-averaged plumes on the (x, z) -plane across the source location for case Wr6-Uc2 ($w_r = 6$ cm/s, $U_c = 2$ cm/s) obtained from LES with different grid numbers $N_x \times N_y \times N_z =$: (a), (d) $240 \times 192 \times 217$; (b), (e) $320 \times 256 \times 289$; (c), (f) $400 \times 320 \times 361$. The top row shows the color contours of the resolved instantaneous dye concentration \bar{C}_{dye} , and the bottom row shows the color contours of the time-averaged vertical velocity \bar{w} . In each panel, the solid lines are the isolines of $\bar{C}_b = 0.001$ kg/m³, which are used to indicate the shape and location of the time-averaged bubble column.

APPENDIX B: GRID RESOLUTION TEST

In this Appendix, the dependence of the LES result on the computational grid resolution is tested based on the plume condition with $w_r = 6$ cm/s and $U_c = 2$ cm/s. The simulation results obtained using the original computational grid $N_x \times N_y \times N_z = 320 \times 256 \times 289$ (i.e., case Wr6-Uc2 in Table I) are compared with those obtained from two additional LES runs with $240 \times 192 \times 217$ grid points (referred to as case Wr6-Uc2-L) and $400 \times 320 \times 361$ grid points (referred to as case Wr6-Uc2-H). Both the instantaneous and time-averaged plumes are compared. In particular, Fig. 27 shows the instantaneous plumes at $t = 100$ s after the bubbles were released, and Fig. 28 shows the time-averaged plumes based on 480 instantaneous plume samples taken between $t = 80$ s and 200 s.

As expected, the LES run using more grid points can directly resolve more detailed turbulent structures in the plume flow than those obtained using fewer grid points [e.g., Figs. 27(c) and 27(f) versus Figs. 27(a) and 27(d)]. Nevertheless, the present LES model was able to capture the essential plume flow physics consistently for all the three different grid resolutions considered here. The time-averaged results shown in Fig. 28 exhibit consistent key characteristics of the plume structure, including the tilted rising/falling double plume structure, the peel height, the lateral expansion of the bubble plume above the peel height, the horizontal intrusion layer, etc. More discussion on these characteristics of plume in crossflow is given in Sec. IV. The grid resolution test presented in this Appendix indicates that the computational grid ($N_x \times N_y \times N_z = 320 \times 256 \times 289$) used in the LES cases reported in this study (see Table I) is sufficient for capturing the plume physics correctly.

- [1] M. Römer, H. Sahling, T. Pape, G. Bohrmann, and V. Spiess, Quantification of gas bubble emissions from submarine hydrocarbon seeps at the Makran continental margin (offshore Pakistan), *J. Geophys. Res. Oceans* **117**, C10015 (2012).
- [2] B. Wang, S. A. Socolofsky, J. A. Breier, and J. S. Seewald, Observations of bubbles in natural seep flares at MC 118 and GC 600 using in situ quantitative imaging, *J. Geophys. Res. Oceans* **121**, 2203 (2016).
- [3] A. Wüest, N. H. Brooks, and D. M. Imboden, Bubble plume model for lake restoration, *Water Resour. Res.* **28**, 3235 (1992).
- [4] T. Asaeda and J. Imberger, Structure of bubble plumes in linearly stratified environments, *J. Fluid Mech.* **249**, 35 (1993).
- [5] S. G. Schladow, Lake destratification by bubble-plume systems: Design methodology, *J. Hydraul. Eng.* **119**, 350 (1993).
- [6] C. J. Lemckert and J. Imberger, Energetic bubble plumes in arbitrary stratification, *J. Hydraul. Eng.* **119**, 680 (1993).
- [7] R. Camilli, C. M. Reddy, D. R. Yoerger, B. A. S. Van Mooy, M. V. Jakuba, J. C. Kinsey, C. P. McIntyre, S. P. Sylva, and J. V. Maloney, Tracking hydrocarbon plume transport and biodegradation at Deepwater Horizon, *Science* **330**, 201 (2010).
- [8] J. S. von Deimling, P. Linke, M. Schmidt, and G. Rehder, Ongoing methane discharge at well site 22/4b (North Sea) and discovery of a spiral vortex bubble plume motion, *Mar. Pet. Geol.* **68**, 718 (2015).
- [9] S. A. Socolofsky and E. E. Adams, Role of slip velocity in the behavior of stratified multiphase plumes, *J. Hydraul. Eng.* **131**, 273 (2005).
- [10] S. A. Socolofsky, E. E. Adams, and C. R. Sherwood, Formation dynamics of subsurface hydrocarbon intrusions following the Deepwater Horizon blowout, *Geophys. Res. Lett.* **38**, L09602 (2011).
- [11] S. A. Socolofsky and E. E. Adams, Liquid volume fluxes in stratified multiphase plumes, *J. Hydraul. Eng.* **129**, 905 (2003).
- [12] S. A. Socolofsky, B. C. Crouse, and E. E. Adams, Multi-phase plumes in uniform, stratified and flowing environments, in *Environmental Fluid Mechanics—Theories and Applications*, edited by H. Shen, A. Cheng, K.-H. Wang, and M. H. Teng (ASCE/Fluids Committee, New York, 2002), pp. 84–125.
- [13] S. A. Socolofsky, T. Bhaumik, and D.-G. Seol, Double-plume integral models for near-field mixing in multiphase plumes, *J. Hydraul. Eng.* **134**, 772 (2008).
- [14] D. Yang, B. Chen, S. A. Socolofsky, M. Chamecki, and C. Meneveau, Large-eddy simulation and parameterization of buoyant plume dynamics in stratified flow, *J. Fluid Mech.* **794**, 798 (2016).
- [15] A. Fabregat Tomàs, A. C. Poje, T. M. Özgökmen, and W. K. Dewar, Dynamics of multiphase turbulent plumes with hybrid buoyancy sources in stratified environments, *Phys. Fluids* **28**, 095109 (2016).
- [16] S. Chu and A. Prosperetti, Bubble plumes in a stratified environment: Source parameters, scaling, intrusion height, and neutral height, *Phys. Rev. Fluids* **2**, 104503 (2017).
- [17] P. D. Yapa and Z. Li, Simulation of oil spills from underwater accidents I: Model development, *J. Hydraul. Res.* **35**, 673 (1997).
- [18] A. L. Dissanayake, J. Gros, and S. A. Socolofsky, Integral models for bubble, droplet, and multiphase plume dynamics in stratification and crossflow, *Environ. Fluid Mech.* **18**, 1167 (2018).
- [19] S. A. Socolofsky and E. E. Adams, Multi-phase plumes in uniform and stratified crossflow, *J. Hydraul. Res.* **40**, 661 (2002).
- [20] M. C. Boufadel, S. Socolofsky, J. Katz, D. Yang, C. Daskiran, and W. Dewar, A review on multiphase underwater jets and plumes: Droplets, hydrodynamics, and chemistry, *Rev. Geophys.* **58**, e2020RG000703 (2020).
- [21] N. G. Deen, T. Solberg, and B. H. Hjertager, Large eddy simulation of the gas–liquid flow in a square cross-sectioned bubble column, *Chem. Eng. Sci.* **56**, 6341 (2001).
- [22] G. Hu and I. Celik, Eulerian–Lagrangian based large-eddy simulation of a partially aerated flat bubble column, *Chem. Eng. Sci.* **63**, 253 (2008).
- [23] M. T. Dhotre, N. G. Deen, B. Niceno, Z. Khan, and J. B. Joshi, Large eddy simulation for dispersed bubbly flows: A review, *Int. J. Chem. Eng.* **2013**, 343276 (2013).
- [24] D. Yang, M. Chamecki, and C. Meneveau, Inhibition of oil plume dilution in Langmuir ocean circulation, *Geophys. Res. Lett.* **41**, 1632 (2014).

- [25] A. Fabregat, W. K. Dewar, T. M. Özgökmen, A. C. Poje, and N. Wienders, Numerical simulations of turbulent thermal, bubble and hybrid plumes, *Ocean Model.* **90**, 16 (2015).
- [26] B. Fraga, T. Stoesser, C. C. K. Lai, and S. A. Socolofsky, A LES-based Eulerian–Lagrangian approach to predict the dynamics of bubble plumes, *Ocean Model.* **97**, 27 (2016).
- [27] B. Fraga and T. Stoesser, Influence of bubble size, diffuser width, and flow rate on the integral behavior of bubble plumes, *J. Geophys. Res. Oceans* **121**, 3887 (2016).
- [28] B. Chen, D. Yang, C. Meneveau, and M. Chamecki, Numerical study of the effects of chemical dispersant on oil transport from an idealized underwater blowout, *Phys. Rev. Fluids* **3**, 083801 (2018).
- [29] C. Meneveau and J. Katz, Scale-invariance and turbulence models for large-eddy simulation, *Annu. Rev. Fluid Mech.* **32**, 1 (2000).
- [30] D. Z. Zhang and A. Prosperetti, Ensemble phase-averaged equations for bubbly flows, *Phys. Fluids* **6**, 2956 (1994).
- [31] D. Z. Zhang and A. Prosperetti, Momentum and energy equations for disperse two-phase flows and their closure for dilute suspensions, *Int. J. Multiphase Flow* **23**, 425 (1997).
- [32] S. A. Socolofsky, E. E. Adams, C. Paris, and D. Yang, How do oil, gas, and water interact near a subsea blowout? *Oceanography* **29**, 64 (2016).
- [33] D. Yang, B. Chen, M. Chamecki, and C. Meneveau, Oil plumes and dispersion in Langmuir, upper-ocean turbulence: Large-eddy simulations and K-profile parameterization, *J. Geophys. Res. Oceans* **120**, 4729 (2015).
- [34] C. Peng, S. Xiao, and D. Yang, Large-eddy simulation model for the effect of gas bubble dissolution on the dynamics of hydrocarbon plume from deep-water blowout, *J. Geophys. Res. Oceans* **125**, e2019JC016037 (2020).
- [35] A. K. Aiyer, D. Yang, M. Chamecki, and C. Meneveau, A population balance model for large eddy simulation of polydisperse droplet evolution, *J. Fluid Mech.* **878**, 700 (2019).
- [36] J. C. McWilliams, P. P. Sullivan, and C.-H. Moeng, Langmuir turbulence in the ocean, *J. Fluid Mech.* **334**, 1 (1997).
- [37] J. A. Polton, J. A. Smith, J. A. MacKinnon, and A. E. Tejada-Martinez, Rapid generation of high-frequency internal waves beneath a wind and wave forced oceanic surface mixed layer, *Geophys. Res. Lett.* **35**, L13602 (2008).
- [38] T. Kukulka, A. J. Plueddemann, J. H. Trowbridge, and P. P. Sullivan, Rapid mixed layer deepening by the combination of Langmuir and shear instabilities: A case study, *J. Phys. Oceanogr.* **40**, 2381 (2010).
- [39] J. Ferry and S. Balachandar, A fast Eulerian method for disperse two-phase flow, *Int. J. Multiphase Flow* **27**, 1199 (2001).
- [40] L. Zheng and P. D. Yapa, Buoyant velocity of spherical and nonspherical bubbles/droplets, *J. Hydraul. Eng.* **126**, 852 (2000).
- [41] R. Clift, J. Grace, and M. E. Weber, *Bubbles, Drops, and Particles* (Dover, New York, 1978).
- [42] J. Smagorinsky, General circulation experiments with the primitive equations: I. The basic experiment, *Mon. Weather Rev.* **91**, 99 (1963).
- [43] D. K. Lilly, The representation of small-scale turbulence in numerical simulation experiments, in *Proc. IBM Scientific Computing Symposium on Environmental Science*, edited by H. H. Goldstine (Yorktown Heights, New York, 1967), pp. 195–210.
- [44] E. Bou-Zeid, C. Meneveau, and M. B. Parlange, A scale-dependent Lagrangian dynamic model for large eddy simulation of complex turbulent flows, *Phys. Fluids* **17**, 025105 (2005).
- [45] M. Antonopoulos-Domis, Large-eddy simulation of a passive scalar in isotropic turbulence, *J. Fluid Mech.* **104**, 55 (1981).
- [46] C.-H. Moeng, A large-eddy-simulation model for the study of planetary boundary-layer turbulence, *J. Atmos. Sci.* **41**, 2052 (1984).
- [47] P. J. Mason, Large-eddy simulation of the convective atmospheric boundary layer, *J. Atmos. Sci.* **46**, 1492 (1989).
- [48] P. P. Sullivan, J. C. McWilliams, and C.-H. Moeng, A subgrid-scale model for large-eddy simulation of planetary boundary-layer flows, *Boundary-Layer Meteor.* **71**, 247 (1994).

- [49] V. Kumar, J. Kleissl, C. Meneveau, and M. B. Parlange, Large-eddy simulation of a diurnal cycle of the atmospheric boundary layer: Atmospheric stability and scaling issues, *Water Resour. Res.* **42**, W06D09 (2006).
- [50] M. Chamecki, C. Meneveau, and M. B. Parlange, Large eddy simulation of pollen transport in the atmospheric boundary layer, *J. Aerosol Sci.* **40**, 241 (2009).
- [51] J. D. Albertson and M. B. Parlange, Surface length scales and shear stress: Implications for land-atmosphere interaction over complex terrain, *Water Resour. Res.* **35**, 2121 (1999).
- [52] M. Chamecki, C. Meneveau, and M. B. Parlange, A hybrid spectral/finite-volume algorithm for large-eddy simulation of scalars in the atmospheric boundary layer, *Boundary-Layer Meteor.* **128**, 473 (2008).
- [53] P. H. Gaskell and A. K. C. Lau, Curvature-compensated convective transport: SMART, a new boundedness-preserving transport algorithm, *Int. J. Numer. Methods Fluids* **8**, 617 (1988).
- [54] M. Chamecki and C. Meneveau, Particle boundary layer above and downstream of an area source: Scaling, simulations, and pollen transport, *J. Fluid Mech.* **683**, 1 (2011).
- [55] Y. Pan, M. Chamecki, and S. A. Isard, Dispersion of heavy particles emitted from area sources in the unstable atmospheric boundary layer, *Boundary-Layer Meteor.* **146**, 235 (2013).
- [56] Y. Pan, M. Chamecki, and S. A. Isard, Large-eddy simulation of turbulence and particle dispersion inside the canopy roughness sublayer, *J. Fluid Mech.* **753**, 499 (2014).
- [57] F. P. Bertolotti, T. Herbert, and P. R. Spalart, Linear and nonlinear stability of the Blasius boundary layer, *J. Fluid Mech.* **242**, 441 (1992).
- [58] P. Schlatter, N. Adams, and L. Kleiser, A windowing method for periodic inflow/outflow boundary treatment of non-periodic flows, *J. Comput. Phys.* **206**, 505 (2005).
- [59] S. Chester, C. Meneveau, and M. B. Parlange, Modeling turbulent flow over fractal trees with renormalized numerical simulation, *J. Comput. Phys.* **225**, 427 (2007).
- [60] S. Chester and C. Meneveau, Renormalized numerical simulation of flow over planar and non-planar fractal trees, *Environ. Fluid Mech.* **7**, 289 (2007).
- [61] R. J. A. M. Stevens, J. Graham, and C. Meneveau, A concurrent precursor inflow method for large eddy simulations and applications to finite length wind farms, *Renew. Energy* **68**, 46 (2014).
- [62] R. J. A. M. Stevens, D. F. Gayme, and C. Meneveau, Effects of turbine spacing on the power output of extended wind-farms, *Wind Energy* **19**, 359 (2016).
- [63] D. W. Murphy, X. Xue, K. Sampath, and J. Katz, Crude oil jets in crossflow: Effects of dispersant concentration on plume behavior, *J. Geophys. Res. Oceans* **121**, 4264 (2016).
- [64] D.-G. Seol, D. B. Bryant, and S. A. Socolofsky, Measurement of behavioral properties of entrained ambient water in a stratified bubble plume, *J. Hydraul. Eng.* **135**, 983 (2009).
- [65] L. Zhao, F. Gao, M. C. Bouffadel, T. King, B. Robinson, K. Lee, and R. Conmy, Oil jet with dispersant: Macro-scale hydrodynamics and tip streaming, *AIChE J.* **63**, 5222 (2017).
- [66] C. C. K. Lai and S. A. Socolofsky, The turbulent kinetic energy budget in a bubble plume, *J. Fluid Mech.* **865**, 993 (2019).
- [67] S. A. Socolofsky, Laboratory experiments of multi-phase plumes in stratification and crossflow, Ph.D. thesis, Massachusetts Institute of Technology, Cambridge, MA (2001).
- [68] R. L. Panton, *Incompressible Flow*, 4th ed. (John Wiley & Sons, Hoboken, NJ, 2013).
- [69] E. Palm, Nonlinear thermal convection, *Annu. Rev. Fluid Mech.* **7**, 39 (1975).
- [70] D. J. Tritton, *Physical Fluid Dynamics*, 2nd ed. (Oxford University Press, Oxford, 1988).
- [71] R. K. Zeytounian, Joseph Boussinesq and his approximation: A contemporary view, *C. R. Mecanique* **331**, 575 (2003).
- [72] D. Livescu, Turbulence with large thermal and compositional density variations, *Annu. Rev. Fluid Mech.* **52**, 309 (2020).